The Astrophysical Journal Supplement Series, 244:33 (35pp), 2019 October https://doi.org/10.3847/1538-4365/ab3bfe

An Hα Imaging Survey of All (Ultra)luminous Infrared Galaxies at Decl. $\geqslant -30°$ in the GOALS Sample

Jun-Jie Jin[1,2], Yi-Nan Zhu[3], Hong Wu[1,2], Feng-Jie Lei[1,2], Chen Cao[4], Xian-Min Meng[1], Zhi-Min Zhou[1], and Man I Lam[5]
[1] Key Laboratory of Optical Astronomy, National Astronomical Observatories, Chinese Academy of Sciences, Beijing 100012, People's Republic of China
hwu@bao.ac.cn, jjjin@bao.ac.cn
[2] School of Astronomy and Space Science University of Chinese Academy of Sciences, Beijing 100012, People's Republic of China
[3] School of Physics and Astronomy, Sun Yat-sen University, Zhuhai 519082, People's Republic of China; zhuyn9@mail.sysu.edu.cn
[4] School of Space Science and Physics, Shandong University, Weihai, Shandong 264209, People's Republic of China
[5] Leibniz-Institut für Astrophsik Potsdam (AIP), An der Sternwarte 16, D-14482 Potsdam, Germany
Received 2019 May 1; revised 2019 August 2; accepted 2019 August 13; published 2019 October 7

Abstract

This paper presents the result of Hα imaging for luminous and ultraluminous infrared galaxies. It is a complete subsample of the Great Observatories All-sky LIRG Survey (GOALS) with decl. $\geqslant -30°$, and consists of 148 galaxies with $\log(L_{\rm IR}/L_{\odot}) \geqslant 11.0$. All the Hα images were carried out using the 2.16 m telescope at the Xinglong Station of the National Astronomy Observatories, Chinese Academy of Sciences (NAOC), during the year from 2006 to 2009. We obtained the pure Hα luminosity for each galaxy and corrected the luminosity for [N II] emission, filter transmission, and extinction. We also classified these galaxies based on their morphology and interaction. We found that the distribution of star-forming regions in these galaxies is related to this classification. As the merging process advanced, these galaxies tended to have a more compact distribution of star-forming regions, higher $L_{\rm IR}$, and warmer IR-color (f_{60}/f_{100}). These results imply that the degree of dynamical disturbance plays an important role in determining the distribution of a star-forming region.

Key words: galaxies: evolution – galaxies: interactions – galaxies: starburst

1. Introduction

Luminous infrared galaxies (LIRGs) and ultraluminous infrared galaxies (ULIRGs) are galaxies with infrared luminosity $\log(L_{\rm IR}/L_{\odot}) \geqslant 10^{11}$ and $\log(L_{\rm IR}/L_{\odot}) \geqslant 10^{12}$, respectively. The research for them began after the successful launch of *Infrared Astronomical Satellite* (*IRAS*) in 1983 (Toomre & Toomre 1972; Toomre 1977; Sanders et al. 1988). These galaxies often show signs of tidal interaction and merger, which lead to the extreme nuclear activity and strong starburst (SB; Barnes & Hernquist 1991, 1992, 1996; Zou et al. 1991; Kim 1995; Veilleux et al. 1995; Sanders & Mirabel 1996; Wu et al. 1998a, 1998b; Zheng et al. 1999; Cui et al. 2001; Xia et al. 2002; Springel et al. 2005; Cao et al. 2006; Wang et al. 2006; Lam et al. 2015).

An important question regarding the nature of (U)LIRGs is what phase do they play in the general evolution of galaxies? Many statistical studies showed that the interaction between galaxies can enhance star formation activity (Kennicutt et al. 1987). And the ULIRGs are associated with the interaction (Zou et al. 1991; Sanders et al. 1988; Wu et al. 1998a, 1998b) as well as active galactic nucleus (AGN) activities (Wu et al. 1998a, 1998b). Theoretical and observational works support an evolution scenario where two gas-rich spiral galaxies merge first and drive material from galaxies disk toward the merger center, triggering star formation activity before dust-enshrouded AGN in the circumnuclear region (Sanders et al. 1988; Barnes & Hernquist 1992; Hopkins et al. 2008; Jin et al. 2018).

Former works showed that the degree of interaction has a great influence on the star formation process in ULIRGs. Hattori et al. (2004) performed an Hα imaging observation for 22 LIRGs and found that the distribution of the star formation region is strongly related to the property of galaxy interactions. Many works also showed that the interaction/merger rate increases with IR luminosity, and nearly all (U)LIRGs show signs of interaction/merger events (Wu et al. 1998b; Kim et al. 2002; Veilleux et al. 2002; Zou et al. 1991). Larson et al. (2016) presented an analysis of morphologies and molecular fractions (MGFs) for 65 LIRGs in the Great Observatories All-sky LIRG Survey (GOALS) sample. They found that the mean MGF for non-interacting LIRGs is much less than that of the intermediate stage in major merger LIRGs.

However, the diversities of star-forming and morphological properties in (U)LIRGs are not fully understood. For example, Sanders & Mirabel (1996) suggested that 20% ∼ 30% of LIRGs with $10^{11}L_{\odot} < L_{\rm IR} < 10^{12}L_{\odot}$ are apparently single galaxies. Rigopoulou et al. (1999) presented a mid-infrared (MIR) spectroscopic survey for 62 ULIRGs and found there is no correlation between the merging process and infrared luminosity ($L_{\rm IR}$), which is contrary to conventional ULIRGs evolutionary scenarios. The numerical simulation showed that the minor merger between gas-rich disks and less massive dwarf galaxies can also produce nuclear starbursts (Hernquist & Mihos 1995).

By using the luminosity (Hα, UV, IR) related to young massive stars, we can get the information of star formation. Among them, the Hα emission is proportional to the number of ionizing photos that are produced by young stars with ages less than ∼10 Myr and masses higher than $17M_{\odot}$ (Watson et al. 2016). Therefore, the Hα emission directly traces the presence of recently formed massive stars. Although former studies yield

many interesting results, their samples are not enough (Hattori et al. 2004) or biased on one type of galaxies (Young et al. 1996; Kim et al. 2013; Theios et al. 2016). GOALS[6] is a subset of the *IRAS* Revised Bright Galaxy Sample (RBGS; Sanders et al. 2003). In order to better understand the properties of (U) LIRGs, we have undertaken an Hα imaging survey of 148 (U) LIRGs selected from GOALS that will help us to study the star formation in the (U)LIRGs.

In this paper, we present the initial result for our Hα imaging survey on 148 GOALS sample galaxies. The layout of this paper is as follow: In Section 2, the sample selection and observation are summarized. In Section 3, we describe the data reduction. And in Section 4, we present the main results of this survey that include the Hα catalog and reduced Hα images. The results based on morphological classification are presented in Section 5, and the discussion is provided in Section 6. At last, a summary of the paper is presented in Section 7. Throughout this paper, we adopt the cosmology $H_0 = 75\,\mathrm{km\,s^{-1}\,Mpc^{-1}}$ and a flat universe where $\Omega_M = 0.3$ and $\Omega_\Lambda = 0.7$.

2. Sample and Observations

2.1. Sample

Sanders et al. (2003) provided a complete flux-limited extragalactic sample (the *IRAS* Revised Bright Galaxy Sample, RBGS) with 60 μm flux densities greater than 5.24 Jy and $|b| > 5°$. Armus et al. (2009) constructed the GOALS sample from RBGS, which includes 181 LIRGs and 21 ULIRGs in the local universe ($z < 0.088$). This sample combines data from NASA's *Spitzer Space Telescope*, *Chandra X-Ray Observatory*, *Hubble Space Telescope* (*HST*), and *Galaxy Evolution Explorer* observatories, together with ground-based data (Armus et al. 2009). Chu et al. (2017) have presented broadband *Herschel* imaging for the entire GOALS sample for all six *Herschel* bands (PACS bands: 70, 100, 160 μm; SPIRE bands: 250, 350, 500 μm). This sample spans a wide range of nuclear spectral types and interaction stages that provide an unbiased picture of the (U)LIRGs in local universe. Out of the original list of 202 sources in the GOALS sample, two objects are omitted. One is NGC 5010, whose $L_{\rm IR}$ drops significantly below the LIRG threshold ($\log(L_{\rm IR}/L_\odot) = 11.0$) due to a revised redshift. The other is IRAS 05223-1908, which is proven to be a young stellar object (Chu et al. 2017).

Our (U)LIRG sample is a subset of the GOALS sample. Considering the observatory site (around 40° north latitude), our sample includes 148 objects with decl. $\geqslant -30°$.

The full sample along with their basic properties are listed in Table 1. The detailed measurements can be found in Armus et al. (2009). Given the poor *IRAS* resolution, sometimes there may be a pair or multiple galaxies within an *IRAS* 3σ uncertainty ellipse. In such a case, we visually examined the region covered by the *IRAS* 3σ uncertainty ellipse in the continuum-subtracted Hα images (achieved after data reduction) and included all obvious objects within this region. The different counterparts in the system are represented by N (north), S (south), E (east), or W (west) in Table 1. There are 10 such galaxy pairs in our sample, and each contains two counterparts. So, in the end, there are total of 158 sources in our sample.

Figure 1 shows the sample distribution of $L_{\rm IR}$ and the recession velocity (cz). The black solid line represents the GOALS sample, and the red dashed line represents our sample. It is clear that the two samples have a similar distribution, and there are no significant differences between them. The cz concentrates in the range of 4000–7000 km s^{-1} corresponding to the redshift from 0.013 to 0.023. The left panel shows the $L_{\rm IR}$ distribution. The number of galaxies decreases rapidly as the $L_{\rm IR}$ increases. Most galaxies in our sample are LIRGs with $\log(L_{\rm IR}/L_\odot)$ lower than 12.0.

2.2. Observations

The observations were carried out on the 2.16 m telescope at the Xinglong Station of the National Astronomical Observatories, CAS. All the galaxies in our sample were taken in dark night between 2006 February and 2009 June. We used BAO Faint Object Spectrograph and Camera (BFOSC), which has 2048×2048 pixel^2 with a pixel scale of 0.″30 and has a field of view (FOV) of $11. \times 11.$ arcmin^2. We adopted a readout noise of 8.6 e$^-$ pixel$^-$ with an average gain of 1.65 e$^-$ ADU$^-$ during the observation. The latest description of updated parameters for BFOSC can be seen in Fan et al. (2016).

To obtain the distribution of the star formation region, we observed with both the narrow Hα filter that covered the shifted Hα emission at the velocity of the target galaxy and the broad *R*-band filter that was used to determine the nearby continuum level. There are a series of narrowband Hα filters, whose center wavelength ranges from 6563 to 7052 Å with an FWHM of about 55 Å. The detailed description of Hα filter can be seen in Lei et al. (2018). The effective wavelength $\lambda_{\rm eff}$ of the broad *R*-band filter is 6407 Å.

For each object, the typically integral time is about 600 s in the *R* band and 3600 s in Hα. Table 1 lists the Hα filters for each source used in observation together with all the other observation information.

3. Data Reduction

3.1. Image Preprocessing

After the observation, we checked the quality of the images by naked eye. The subsequent data reduction was performed using IRAF, including overscan subtraction, bias subtraction, and flat-field correction. The cosmic rays were identified and removed using L.A.Cosmic (van Dokkum 2001). Then, the celestial coordinate was added to each image using *Astrometry.net*[7] and the bad columns were replaced with a linear fit of surrounding pixels.

The next step is sky subtraction. The most critical step is the sky background construction. First, Sextractor was employed to detect objects. Before detecting, we produced a Gaussian smoothed image by convolving original images with a Gaussian function of FWHM = 3 pixels to make the area of the objects more extended. If the original image (Figure 2(a)) is directly used for Sextractor to detect objects, it may be hard to derive a good object-masked image because the wings of bright objects cannot be completely masked (Du et al. 2015). Second, we got the object-masked image by subtracting all of the detected objects according to their masked areas from the original image. Third, we used the method provided by Lei et al. (2018) to get a reliable large-scale structure of the background by using this object-masked image. We applied a median filter of 70×70 pixel^2 to convolve the object-masked

[6] http://goals.ipac.caltech.edu

[7] http://nova.astrometry.net

Table 1
The Main Parameter and Observation Information of Our Source

(1) Name	(2) R.A. J2000	(3) Decl. J2000	(4) cz (km s^{-1})	(5) Dist[a] (Mpc)	(6) $F(25\ \mu m)$ (Jy)	(7) $F(60\ \mu m)$ (Jy)	(8) $F(100\ \mu m)$ (Jy)	(9) L_{IR}[b] ($L_\odot$)	(10) Filter[c]	(11) Date	(12) Seeing (arcsec)
Arp220	15:34:57.12	+23:30:11.5	5434	87.9	8.0	104.09	115.29	12.28	c3	2007 May 15	2.7
CGCG 011-076	11:21:12.26	−02:59:03.5	7464	117.0	0.76	5.85	9.18	11.43	c4	2007 Apr 17	2.4
CGCG 043-099	13:01:50.80	+04:20:00.0	11237	175.0	0.47	5.25	8.06	11.68	c6	2008 Feb 13	2.1
CGCG 049-057	15:13:13.09	+07:13:31.8	3897	65.4	0.95	21.89	31.53	11.35	c3	2007 Mar 17	2.2
CGCG 052-037	16:30:56.54	+04:04:58.4	7342	116.0	0.81	7.00	11.23	11.45	c4	2008 Apr 3	2.0
CGCG 141-034	17:56:56.63	+24:01:01.6	5944	93.4	0.56	6.24	10.55	11.20	c4	2006 Jul 22	3.0
CGCG 142-034	18:16:40.66	+22:06:46.1	5599	88.1	0.55	6.25	11.94	11.18	c4	2006 Jul 21	2.2
CGCG 247-020	14:19:43.25	+49:14:11.7	7716	120.0	0.84	6.01	8.47	11.39	c4	2007 Feb 23	3.0
CGCG 436-030	01:20:02.72	+14:21:42.9	9362	134.0	1.54	10.71	9.67	11.69	c5	2007 Sep 10	2.5
CGCG 448-020	20:57:23.90	+17:07:39.0	10822	161.0	2.30	12.65	11.76	11.94	c6	2007 Sep 9	2.5
CGCG 453-062	23:04:56.53	+19:33:08.0	7524	109.0	0.54	7.19	11.73	11.38	c4	2006 Sep 25	3.2
CGCG 465-012	03:54:16.08	+15:55:43.4	6662	94.3	0.75	5.65	8.95	11.20	c4	2007 Feb 15	2.0
CGCG 468-002	05:08:20.50	+17:21:58.0	5454	77.9	1.16	9.66	14.59	11.22	c3	2008 Feb 10	2.1
ESO 453-G005	16:47:31.06	−29:21:21.6	6260	100.0	0.61	9.56	12.17	11.37	c4	2008 Jun 4	2.4
ESO 467-G027	22:14:39.92	−27:27:50.3	5217	77.3	0.58	5.58	12.48	11.08	c3	2007 Nov 10	2.1
ESO 507-G070	13:02:52.35	−23:55:17.7	6506	106.0	0.80	13.04	15.71	11.56	c4	2007 Feb 14	3.4
ESO 550-IG02(N)	04:21:20.02	−18:48:47.6	9621	138.5	0.27	3.05	5.08	11.24	c5	2007 Feb 14	3.4
ESO 550-IG02(S)	04:21:20.02	−18:48:47.6	9621	138.5	0.24	2.64	4.39	11.18	c5	2007 Nov 10	1.8
ESO 557-G002	06:31:47.22	−17:37:17.3	6385	93.6	0.86	7.42	10.50	11.25	c4	2007 Feb 14	2.2
ESO 593-IG008	19:14:30.90	−21:19:07.0	14608	222.0	0.51	6.38	9.37	11.93	c7	2008 Jun 7	2.4
ESO 602-G025	22:31:25.48	−19:02:04.1	7507	110.0	0.91	5.42	9.64	11.34	c4	2007 Oct 11	2.6
IC 0214	02:14:05.59	+05:10:23.7	9061	129.0	0.62	5.28	8.57	11.43	c5	2007 Nov 10	2.4
IC 0860	13:15:03.53	+24:37:07.9	3347	56.8	1.34	18.61	18.66	11.14	c3	2007 Feb 14	2.1
IC 1623A	01:07:47.18	−17:30:25.3	6016	85.5	3.65	22.93	31.55	11.71	c4	2007 Nov 11	2.5
IC 2810	11:25:47.30	+14:40:21.1	10192	157.0	0.62	6.20	10.39	11.64	c6	2007 Feb 15	2.2
IC 4280	13:32:53.40	−24:12:25.7	4889	82.4	0.68	6.10	12.36	11.15	c3	2008 Feb 7	4.2
IC 5298	23:16:00.70	+25:33:24.1	8221	119.0	1.95	9.06	11.99	11.60	c5	2008 Sep 29	1.8
IC 563	09:46:20.71	+03:03:30.5	5996	92.9	0.27	2.68	6.18	10.94	c4	2007 Apr 17	2.1
IC 564	09:46:20.71	+03:03:30.5	5996	92.9	0.27	2.59	6.00	10.92	c4	2007 Apr 17	2.1
III Zw 035(N)	01:44:30.45	+17:06:05.0	8375	119.0	0.52	6.63	7.15	11.3	c5	2007 Sep 10	2.1
III Zw 035(S)	01:44:30.45	+17:06:05.0	8375	119.0	0.51	6.62	7.15	11.3	c5	2007 Sep 10	2.1
IRAS 03582+6012	04:02:32.48	+60:20:40.1	8997	131.0	0.70	5.65	7.76	11.43	c5	2007 Nov 12	2.1
IRAS 04271+3849	04:30:33.09	+38:55:47.7	5640	80.8	0.74	6.53	10.36	11.11	c4	2008 Feb 7	2
IRAS 05083+2441	05:11:25.88	+24:45:18.3	6915	99.2	0.85	6.92	8.36	11.26	c4	2007 Feb 23	2.4
IRAS 05129+5128	05:16:56.10	+51:31:56.5	8224	120.0	1.05	6.56	7.34	11.42	c5	2007 Feb 23	2.3
IRAS 05442+1732	05:47:11.18	+17:33:46.7	5582	80.5	1.70	10.02	12.73	11.30	c4	2007 Feb 14	1.6
IRAS 17578-0400	18:00:31.90	−04:00:53.3	4210	68.5	1.14	27.69	33.1	11.48	c3	2007 Oct 10	3.3
IRAS 18090+0130	18:11:35.91	+01:31:41.3	8662	134.0	0.81	7.73	15.64	11.65	c5	2007 Oct 11	2.0
IRAS 19542+1110	19:56:35.44	+11:19:02.6	19473	295.0	0.77	6.18	6.22	12.12	c10	2008 Jun 6	3.0
IRAS 20351+2521	20:37:17.72	+25:31:37.7	10102	151.0	0.71	5.93	8.95	11.61	c5	2007 Sep 10	3.0
IRAS 21101+5810	21:11:30.40	+58:23:03.2	11705	174.0	0.82	7.94	11.08	11.81	c6	2008 Sep 29	2.0
IRAS 23436+5257	23:46:05.58	+53:14:00.6	10233	149.0	0.74	5.66	9.01	11.57	c6	2008 Sep 29	1.7
IRAS F01364-1042	01:38:52.92	−10:27:11.4	14464	210.0	0.44	6.62	6.88	11.85	c7	2008 Sep 28	3.3
IRAS F02437+2122	02:46:39.15	+21:35:10.3	6987	98.8	0.63	5.90	6.67	11.16	c4	2007 Sep 9	2.5
IRAS F03217+4022	03:25:05.38	+40:33:29.0	7007	100.0	0.91	7.47	10.87	11.33	c4	2007 Nov 12	2.1
IRAS F03359+1523	03:38:46.70	+15:32:55.0	10613	152.0	0.65	5.97	7.27	11.55	c6	2007 Nov 10	1.5
IRAS F05187-1017	05:21:06.54	−10:14:46.7	8474	122.0	0.19	5.39	8.04	11.30	c5	2007 Mar 17	2.5
IRAS F05189-2524	05:21:01.47	−25:21:45.4	12760	187.0	3.47	13.25	11.84	12.16	c7	2008 Feb 14	2.5
IRAS F06076-2139	06:09:45.81	−21:40:23.7	11226	165.0	0.63	6.43	8.47	11.65	c6	2008 Feb 8	3.0
IRAS F08339+6517	08:38:23.18	+65:07:15.2	5730	86.3	1.13	5.81	6.48	11.11	c4	2007 Nov 6	1.5
IRAS F08572+3915	09:00:25.39	+39:03:54.4	17493	264.0	1.76	7.30	4.77	12.16	c9	2008 Feb 13	1.5
IRAS F09111-1007	09:13:37.61	−10:19:24.8	16231	246.0	0.74	6.75	10.68	12.06	c8	2008 Feb 13	1.5
IRAS F10173+0828	10:20:00.21	+08:13:33.8	14716	224.0	0.55	5.61	5.86	11.86	c7	2008 Feb 14	1.8
IRAS F10565+2448	10:59:18.14	+24:32:34.3	12921	197.0	1.27	12.10	15.01	12.08	c7	2008 Feb 14	1.8
IRAS F12112+0305	12:13:46.00	+02:48:38.0	21980	340.0	0.66	8.18	9.46	12.36	c11	2008 Feb 13	1.8
IRAS F12224-0624	12:25:03.91	−06:40:52.6	7902	125.0	0.20	5.99	8.13	11.36	c5	2008 Jan 31	2.3
IRAS F15250+3608	15:26:59.40	+35:58:37.5	16535	254.0	1.31	7.10	5.93	12.08	c8	2008 Feb 13	2.7
IRAS F16164-0746	16:19:11.79	−07:54:02.8	8140	128.0	0.59	10.29	13.22	11.62	c5	2008 Feb 9	3.3
IRAS F16399-0937	16:42:40.21	−09:43:14.4	8098	128.0	1.13	8.42	14.72	11.63	c5	2008 Feb 9	2.7
IRAS F16516-0948	16:54:24.03	−09:53:20.9	6755	107.0	0.49	5.32	11.65	11.31	c4	2008 May 2	2.1
IRAS F17132+5313	17:14:20.00	+53:10:30.0	15270	232.0	0.65	6.07	7.90	11.96	c8	2007 Nov 12	1.8
IRAS F17138-1017	17:16:35.79	−10:20:39.4	5197	84.0	2.12	15.18	19.02	11.49	c3	2007 Sep 8	1.8

Table 1
(Continued)

(1) Name	(2) R.A. J2000	(3) Decl. J2000	(4) cz (km s^{-1})	(5) Dist[a] (Mpc)	(6) $F(25\ \mu m)$ (Jy)	(7) $F(60\ \mu m)$ (Jy)	(8) $F(100\ \mu m)$ (Jy)	(9) L_{IR}[b] ($L_\odot$)	(10) Filter[c]	(11) Date	(12) Seeing (arcsec)
IRAS F17207-0014	17:23:21.95	−00:17:00.9	12834	198.0	1.61	32.13	36.08	12.46	c7	2008 May 2	2.6
IRAS F22491-1808	22:51:49.26 s	−17:52:23.5	23312	351.0	0.54	5.54	4.64	12.20	c11	2008 Sep 28	4.0
IRAS F23365+3604	23:39:01.27	+36:21:08.7	19331	287.0	0.94	7.44	9.01	12.20	c10	2007 Nov 11	2.5
MCG+02-20-003	07:35:43.37	+11:42:33.5	4873	72.8	0.81	9.38	13.33	11.13	c3	2009 Jan 17	2.5
MCG+04-48-002	20:28:35.06	+25:44:00.0	4167	64.2	1.09	9.93	17.36	11.11	c3	2006 Sep 23	1.6
MCG+05-06-036	02:23:21.99	+32:11:49.5	10106	145.0	0.80	6.55	11.63	11.64	c5	2007 Nov 11	2.5
MCG+07-23-019	11:03:53.20	+40:50:57.0	10350	158.0	0.71	6.38	10.30	11.62	c6	2007 Feb 23	2.5
MCG+08-11-002	05:40:43.71	+49:41:41.5	5743	83.7	1.08	14.03	24.82	11.46	c4	2007 Feb 14	1.7
MCG+08-18-013	09:36:37.19	+48:28:27.7	7777	117.0	0.75	5.68	8.42	11.34	c4	2008 Feb 6	2.4
MCG+12-02-001	00:54:03.61	+73:05:11.8	4706	69.8	3.51	21.92	29.11	11.50	c3	2007 Sep 8	1.8
MCG-02-01-051	00:18:50.51	−10:22:09.2	8159	117.5	0.66	4.11	5.31	11.22	c5	2007 Oct 10	3.0
MCG-02-01-052	00:18:50.51	−10:22:09.2	8159	117.5	0.54	3.37	4.35	11.13	c5	2007 Oct 10	3.0
MCG-02-33-098	13:02:19.70	−15:46:03.0	4773	78.7	1.63	7.49	9.68	11.17	c3	2007 Feb 15	2.0
MCG-03-04-014	01:10:08.96	−16:51:09.8	10040	144.0	0.90	7.25	10.33	11.65	c6	2007 Nov 10	1.8
MCG-03-34-064	13:22:24.46	−16:43:42.9	4959	82.2	2.97	6.20	6.20	11.28	c3	2008 Feb 7	3.0
MCG01-60-022	23:42:00.85	−03:36:54.6	6966	100.0	1.06	5.39	8.26	11.27	c4	2007 Sep 9	3.0
Mrk231	12:56:14.24	+56:52:25.2	12642	192.0	8.84	30.80	29.74	12.57	c6	2007 Apr 17	2.4
Mrk331	23:51:26.80	+20:35:09.9	5541	79.3	2.54	18.00	22.70	11.50	c3	2007 Sep 8	1.8
NGC 0317B	00:57:40.45	+43:47:32.1	5429	77.8	1.03	9.16	13.60	11.19	c3	2007 Sep 8	1.8
NGC 0838	02:09:38.58	−10:08:46.3	3851	53.8	1.88	11.41	19.94	11.05	c3	2007 Sep 8	1.8
NGC 0958	02:30:42.83	−02:56:20.4	5738	80.6	0.94	5.85	15.08	11.20	c4	2007 Feb 15	2.5
NGC 0992	02:37:25.49	+21:06:03.0	4141	58.0	1.76	11.40	16.72	11.07	c3	2007 Feb 14	1.7
NGC 1068	02:42:40.71	−00:00:47.8	1137	15.9	87.57	196.37	257.37	11.40	c1	2007 Feb 14	2.1
NGC 1275	03:19:48.16	+41:30:42.1	5264	75.0	3.44	6.99	7.2	11.26	c3	2009 Jan 29	2.0
NGC 1614	04:33:59.85	−08:34:44.0	4778	67.8	7.50	32.12	34.32	11.65	c3	2007 Nov 10	1.5
NGC 1797	05:07:44.88	−08:01:08.7	4441	63.4	1.35	9.56	12.76	11.04	c3	2008 Feb 7	2.1
NGC 1961	05:42:04.65	+69:22:42.4	3934	59.0	0.99	7.17	23.37	11.06	c3	2007 Oct 11	2.0
NGC 2146	06:18:37.71	+78:21:25.3	893	17.5	18.81	146.69	194.05	11.12	c1	2007 Mar 16	2.5
NGC 23	00:09:53.41	+25:55:25.6	4566	65.2	1.29	9.03	15.66	11.12	c3	2006 Sep 22	2.0
NGC 232	00:42:45.82	−23:33:40.9	6647	95.2	1.28	10.05	17.14	11.44	c4	2007 Oct 10	2.5
NGC 2342	07:09:18.08	+20:38:09.5	5276	78.0	1.64	7.73	24.10	11.31	c3	2007 Mar 13	1.9
NGC 2388	07:28:53.44	+33:49:08.7	4134	62.1	1.98	16.74	24.58	11.28	c3	2006 Feb 23	3.9
NGC 2623	08:38:24.08	+25:45:16.6	5549	84.1	1.81	23.74	25.88	11.60	c3	2007 Mar 17	2.3
NGC 3110	10:04:02.11	−06:28:29.2	5054	79.5	1.13	11.28	22.27	11.37	c3	2007 Mar 13	2.3
NGC 3221	10:22:19.98	+21:34:10.5	4110	65.7	0.93	7.72	18.76	11.09	c3	2006 Feb 22	2.6
NGC 34	00:11:06.55	−12:06:26.3	5881	84.1	2.39	17.05	16.86	11.49	c4	2007 Oct 11	2.8
NGC 3690(E)	11:28:32.25	+58:33:44.0	3093	50.7	11.98	55.28	54.48	11.62	c2	2007 Mar 17	2.0
NGC 3690(W)	11:28:32.25	+58:33:44.0	3093	50.7	12.53	57.77	56.94	11.64	c2	2007 Mar 17	2.0
NGC 4194	12:14:09.47	+54:31:36.6	2501	43.0	4.51	23.20	25.16	11.10	c2	2008 Feb 9	2.1
NGC 4418	12:26:54.62	−00:52:39.2	2179	36.5	9.67	43.89	31.94	11.19	c2	2007 Feb 14	2.3
NGC 4922	13:01:24.89	+29:18:40.0	7071	111.0	1.48	6.21	7.33	11.38	c4	2008 Feb 9	2.4
NGC 5104	13:21:23.08	+00:20:32.7	5578	90.8	0.74	6.78	13.37	11.27	c4	2007 Feb 23	2.8
NGC 5135	13:25:44.06	−29:50:01.2	4105	60.9	2.38	16.86	30.97	11.30	c3	2008 Feb 12	4.2
NGC 5256	13:38:17.52	+48:16:36.7	8341	129.0	1.07	7.25	10.11	11.56	c5	2007 Feb 24	1.9
NGC 5257	13:39:55.00	+00:50:07.0	6778	108.5	0.76	6.11	11.36	11.38	c4	2007 Mar 17	1.9
NGC 5258	13:39:55.00	+00:50:07.0	6778	108.5	0.58	4.62	8.61	11.25	c4	2007 Mar 17	1.9
NGC 5331	13:52:16.29	+02:06:17.0	9906	155.0	0.59	5.86	11.49	11.66	c5	2007 Mar 14	2.2
NGC 5394	13:58:35.81	+37:26:20.3	3482	58.7	0.61	4.09	9.59	10.72	c3	2007 Feb 14	2.1
NGC 5395	13:58:35.81	+37:26:20.3	3482	58.7	0.79	5.30	12.43	10.83	c3	2007 Feb 14	2.1
NGC 5653	14:30:10.42	+31:12:55.8	3562	60.2	1.37	10.57	23.03	11.13	c3	2007 Feb 14	2.3
NGC 5734	14:45:09.05	−20:52:13.7	4121	67.1	0.74	7.99	24.79	11.15	c3	2007 Mar 17	2.9
NGC 5936	15:30:00.84	+12:59:21.5	4004	67.1	1.47	8.73	17.66	11.14	c3	2006 Jul 2	2.1
NGC 5990	15:46:16.37	+02:24:55.7	3839	64.4	1.60	9.59	17.14	11.13	c3	2007 Mar 16	1.8
NGC 6052	16:05:13.05	+20:32:32.6	4739	77.6	0.83	6.79	10.57	11.09	c3	2006 Jul 5	3.9
NGC 6090	16:11:40.70	+52:27:24.0	8947	137.0	1.24	6.48	9.41	11.58	c5	2008 May 2	1.8
NGC 6240	16:52:58.89	+02:24:03.4	7339	116.0	3.55	22.94	26.49	11.93	c4	2008 Feb 8	5.0
NGC 6286	16:58:31.38	+58:56:10.5	5501	85.7	0.62	9.24	23.11	11.37	c4	2006 Jul 2	2.9
NGC 6621	18:12:55.31	+68:21:48.4	6191	94.3	0.97	6.78	12.01	11.29	c4	2007 May 15	2.5
NGC 6670(E)	18:33:35.91	+59:53:20.2	8574	129.5	0.52	4.46	7.05	11.35	c5	2006 Jul 22	2.4
NGC 6670(W)	18:33:35.91	+59:53:20.2	8574	129.5	0.53	4.52	7.14	11.35	c5	2006 Jul 22	2.4
NGC 6701	18:43:12.46	+60:39:12.0	3965	62.4	1.32	10.05	20.05	11.12	c3	2006 Jul 22	2.7
NGC 6786	19:10:59.20	+73:25:06.3	7528	113.0	1.42	7.58	10.77	11.49	c4	2006 Sep 22	1.9

Table 1
(Continued)

(1) Name	(2) R.A. J2000	(3) Decl. J2000	(4) cz (km s^{-1})	(5) Dist[a] (Mpc)	(6) $F(25\ \mu m)$ (Jy)	(7) $F(60\ \mu m)$ (Jy)	(8) $F(100\ \mu m)$ (Jy)	(9) L_{IR}[b] ($L_\odot$)	(10) Filter[c]	(11) Date	(12) Seeing (arcsec)
NGC 6907	20:25:06.65	−24:48:33.5	3190	50.1	1.94	14.14	29.59	11.11	c2	2007 Nov 11	2.5
NGC 6926	20:33:06.11	−02:01:39.0	5880	89.1	1.03	7.09	14.38	11.32	c4	2006 Sep 23	1.9
NGC 695	01:51:14.24	+22:34:56.5	9735	139.0	0.83	7.59	13.56	11.68	c5	2007 Sep 10	2.1
NGC 7469	23:03:15.62	+08:52:26.4	4892	70.8	5.96	27.33	35.16	11.65	c3	2007 Sep 8	1.8
NGC 7591	23:18:16.28	+06:35:08.9	4956	71.4	1.27	7.87	14.87	11.12	c3	2006 Sep 22	2.3
NGC 7592(E)	23:18:22.20	−04:24:57.6	7328	106.0	0.55	4.60	6.04	11.16	c4	2007 Sep 9	3.0
NGC 7592(W)	23:18:22.20	−04:24:57.6	7328	106.0	0.42	3.46	4.54	11.03	c4	2007 Sep 9	3.0
NGC 7674	23:27:56.72	+08:46:44.5	8671	125.0	1.92	5.36	8.33	11.56	c5	2007 Sep 10	3.0
NGC 7679	23:28:46.66	+03:30:41.1	5138	73.8	1.12	7.40	10.71	11.11	c3	2007 Sep 8	1.5
NGC 7752	23:47:01.70	+29:28:16.3	5120	73.6	0.46	3.20	6.40	10.81	c3	2008 Sep 29	1.7
NGC 7753	23:47:01.70	+29:28:16.3	5120	73.6	0.37	2.59	5.18	10.72	c3	2008 Sep 29	1.7
NGC 7771	23:51:24.88	+20:06:42.6	4277	61.2	2.17	19.67	40.12	11.40	c3	2006 Sep 22	2.1
NGC 828	02:10:09.57	+39:11:25.3	5374	76.3	1.07	11.46	25.33	11.36	c3	2006 Sep 22	2.0
NGC 877	02:17:59.64	+14:32:38.6	3913	54.6	1.41	11.82	25.56	11.10	c3	2006 Sep 23	2.0
UGC 01385	01:54:53.79	+36:55:04.6	5621	79.8	0.99	5.89	7.81	11.05	c4	2007 Feb 15	2
UGC 03410	06:14:29.63	+80:26:59.6	3921	59.7	0.92	9.87	22.98	11.10	c3	2009 Jan 18	1.8
UGC 04881	09:15:55.11	+44:19:54.1	11851	178.0	0.61	6.07	10.33	11.74	c6	2007 Feb 15	2.3
UGC 08387	13:20:35.34	+34:08:22.2	6985	110.0	1.42	17.04	24.38	11.73	c4	2007 Feb 15	2
UGC 08739	13:49:13.93	+35:15:26.8	5032	81.4	0.42	5.79	15.89	11.15	c3	2007 Feb 15	1.4
UGC 11041	17:54:51.82	+34:46:34.4	4881	77.5	0.69	5.84	12.78	11.11	c3	2006 Jul 5	3.5
UGC 12150	22:41:12.26	+34:14:57.0	6413	93.5	0.82	8.00	15.58	11.35	c4	2006 Jul 22	2.2
UGC 1845	02:24:07.98	+47:58:11.0	4679	67.0	1.07	10.31	15.51	11.12	c3	2007 Oct 11	2.4
UGC 2238	02:46:17.49	+13:05:44.4	6560	92.4	0.65	8.17	15.67	11.33	c4	2006 Sep 22	2.3
UGC 2369	02:54:01.78	+14:58:24.9	9558	136.0	1.88	8.07	11.18	11.67	c5	2006 Sep 23	2.0
UGC 2608	03:15:01.42	+42:02:09.4	6998	100.0	1.45	8.18	11.27	11.41	c4	2008 Feb 6	2.1
UGC 2982	04:12:22.45	+05:32:50.6	5305	74.9	0.83	8.39	16.82	11.20	c3	2007 Oct 11	3.0
UGC 3094	04:35:33.83	+19:10:18.2	7408	106.0	0.84	6.35	12.85	11.41	c4	2007 Nov 6	1.4
UGC 3351	05:45:47.88	+58:42:03.9	4455	65.8	0.86	14.26	29.46	11.28	c3	2008 Sep 29	1.8
UGC 3608	06:57:34.45	+46:24:10.8	6401	94.3	1.20	8.05	11.33	11.34	c4	2007 Nov 6	1.5
UGC 5101	09:35:51.65	+61:21:11.3	11802	177.0	1.02	11.68	19.91	12.01	c6	2008 Feb 7	2.4
VII ZW 031	05:16:46.44	+79:40:12.6	16090	240.0	0.62	5.51	10.09	11.99	c8	2007 Nov 12	2.5
VV250a	13:15:35.06	+62:07:28.6	9313	142.0	1.95	11.39	12.41	11.81	c5	2007 May 16	1.8
VV340a	14:57:00.68	+24:37:02.7	10094	157.0	0.41	6.95	15.16	11.74	c5	2007 Jul 1	2.1
VV705	15:18:06.28	+42:44:41.2	11944	183.0	1.42	9.02	10.00	11.92	c6	2007 Apr 17	2.1

Notes.
[a] For most objects this was calculated from cz using the cosmic attractor model (Mould et al. 2000) with $H_0 = 75$ km s^{-1} Mpc^{-1} and a flat universe where $\Omega_M = 0.3$ and $\Omega_\Lambda = 0.7$.
[b] The log of the 8–1000 micron luminosity determined using all *IRAS* bands with the units of solar bolometric luminosity ($L_\odot = 3.83 \times 10^{33}$ srg s^{-1}).
[c] Hα filter used in observation.

image in order to reduce the random noise and to fill in the mask regions by the surrounding sky region. Unfortunately, due to the fact that our objects are too large, the backgrounds in the center of the sources are not filled (Figure 2(b)). We adopted two methods to deal with this problem.

We found that the background of our images had a similar pattern in the same filter. We conducted image combination with a 3σ clip to get an average background for each filter, which removed most signatures for the regions masked incompletely, such as the unfilled region as well as the wings of the bright stars (Figure 2(c)). The average background was then scaled and subtracted from the original image. Figure 2(d) shows an example of the sky-subtracted image.

There were still some images with a strange pattern so that we could not get the background by this method, and therefore we made the background as done by Zheng et al. (1999), Wu et al. (2002), and Du et al. (2015). We performed a least-squares polynomial fit of low order to the sky pixels of each row and column and then averaged the line-fitted and column-fitted images to get the averaged background. At last this averaged image (Figure 2(f)) was smoothed with a Gaussian function of FWHM = 31 pixels (Figure 2(g)) and used as sky background. Figure 2(h) shows the sky-subtracted example for the second method.

The sky backgrounds derived from these two methods both show the vignetting and nonuniformity distribution. Figures 3(a) and (b) show the fluctuation of two example images for method-1 and method-2. It is clear that the mean values of the Gaussian distribution for images with our sky background subtraction are close to zero and have much less fluctuation than those of the original images.

Then the Hα images were scaled relative to the continuum *R*-band images using field stars, and the continuum *R*-band images were subtracted from the scaled Hα image to yield continuum-free images. In this process, we assume the absence of feature lines on their continua of the field stars. The scaling factors are defined by

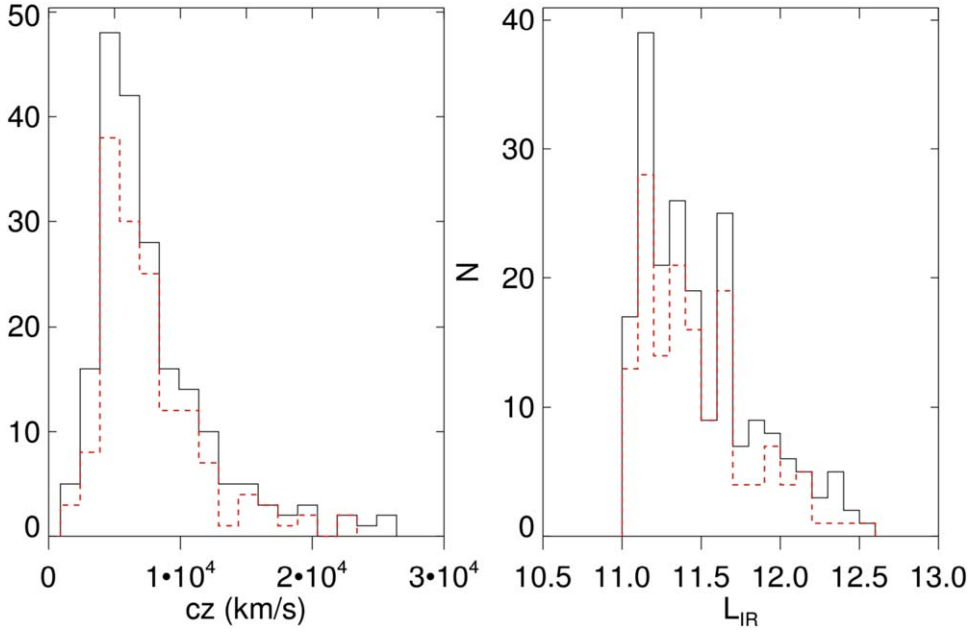

Figure 1. Distribution of cz and L_{IR} of GOALS and our sample. The black solid lines represent GOALS, and the red dashed lines represent our sample.

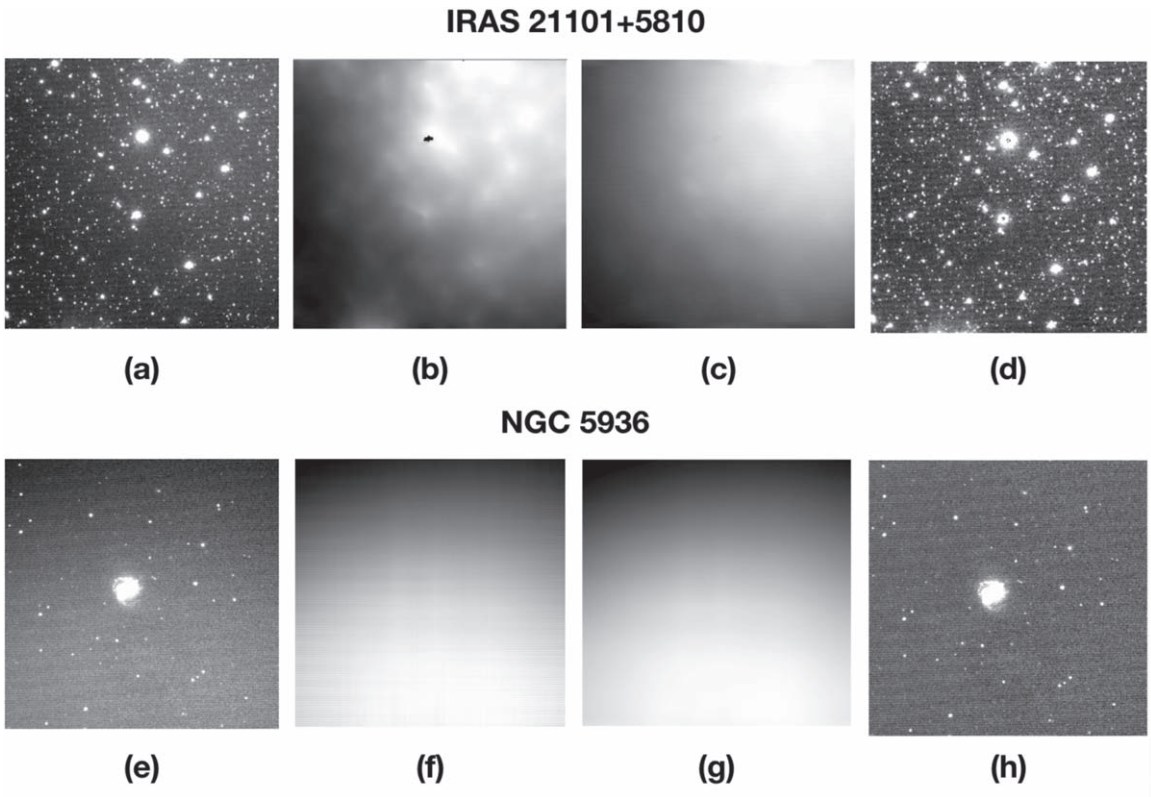

Figure 2. Example of sky subtraction. Top panel: sky-subtraction process for LIRGs IRAS 21101+5810 (method-1). The four panels show the (a) original image; (b) the sky background directly from the original image; (c) average stacking sky background; (d) sky-subtracted image. Bottom panel: sky-subtraction process for NGC 5936 (method-2). The four panels show the (e) original image; (f) the average sky image of the row-fitted and column-fitted sky image; (g) the smoothed sky background image; (h) sky-subtracted image.

the ratio between counts of field stars in the wide *R* band and narrow Hα band. We adopt the median value first and then adjust the value around until the residual fluxes of foreground stars reached the minimum. Figure 4 shows the Hα-band, *R*-band, and continuum-subtracted Hα images of NGC 5394/5 as an example.

3.2. Photometry

The continuum-subtracted Hα images were flux calibrated using photometry from the Panoramic Survey Telescope and Rapid Response System (Pan-STARRS). The Pan-STARRS survey is designed for collecting wide-field astronomical

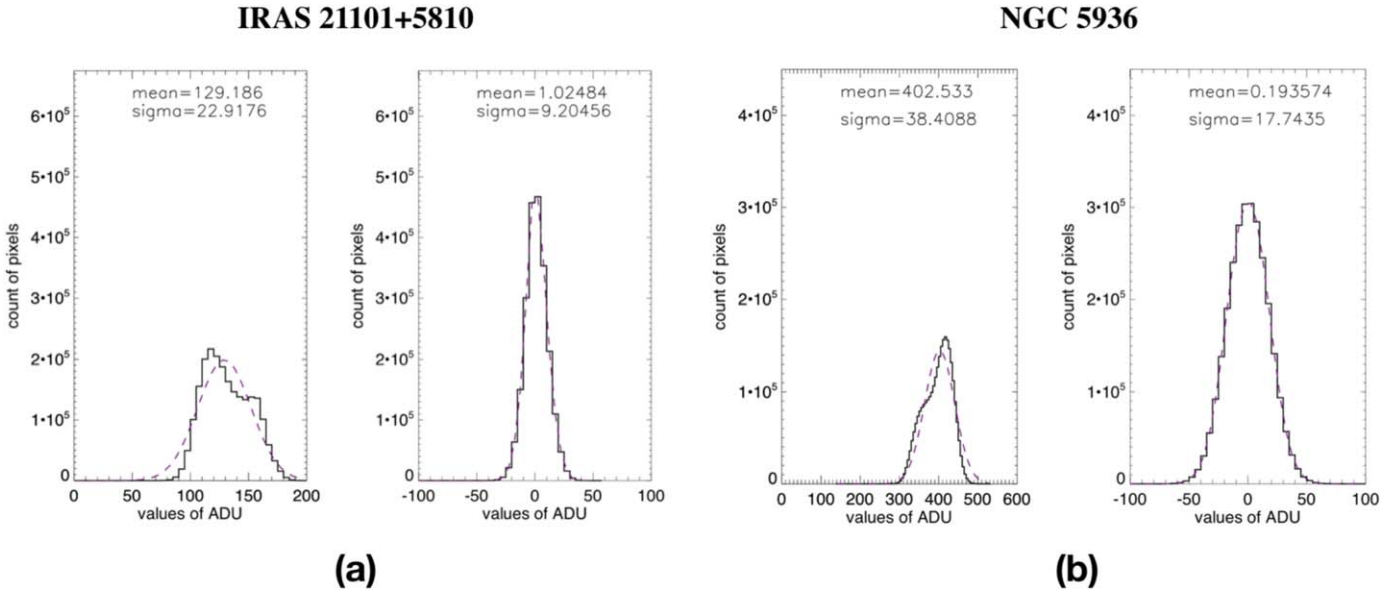

Figure 3. Example of count distribution before and after sky subtraction. The left panels of (a) and (b) represent the count distribution for all unmasked pixels in the original image of RAS 21101+5810 in Hα-6 (method-1) and NGC 5936 in Hα-3 (method-2), respectively. The right panels of (a) and (b) represent the count distribution for all unmasked pixels in the sky-subtracted image. The mean value and standard deviation of the distribution are given at the top of each panel.

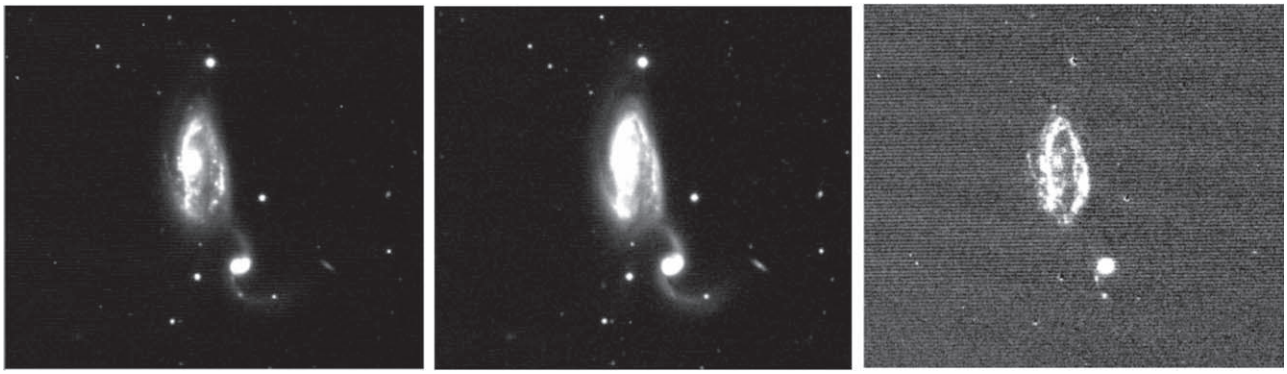

Figure 4. Example of continuum-subtracted images. The Hα-band, *R*-band, and continuum-subtracted Hα images of LIRGs NGC 5394/5 are shown from left to right.

imaging and operated by the Institute for Astronomy at the University of Hawaii. This survey used a 1.8 m telescope with a 1.4 Gigapixel camera to image the sky in five broadband filters (*g, r, i, z, y*). The systematic errors in the Pan-STARRS photometric system are about 0.02 mag (Tonry et al. 2012). In our work, the Pan-STARRS's point-spread function magnitudes of the *g* band (m_g) and *r* band (m_r) were used to get the Johnson/Cousins *R*-band magnitude (m_R) with the formula given by Tonry et al. (2012):

$$m_R - m_r = -0.138 - 0.131(m_g - m_r) \pm 0.015.$$

Then m_R is transformed to flux density with the following equation (Oke & Gunn 1983; Frei & Gunn 1994):

$$m_{AB} = m_R + 0.055,$$
$$m_{AB} = -2.5\log_{10}\left(\frac{f_\nu}{3631JY}\right).$$

Then by comparing the field star in our observation and Pan-STARRS, we derived the flux calibration in this observation.

Before the photometry, field stars must be masked in *R*-band images. The *Sextractor* was used to find stars across the image and replace them with the median of background value. The counterparts of the galaxy pair were masked in a similar way. When we measure one object, the other is masked, as in the example shown in Figure 5. The continuum-subtracted Hα images also require masking in the case where the galaxy pair or the residuals from star were not subtracted clearly. The $L_{\rm IR}$ was also assigned into two counterparts of galaxy pairs according to their Hα fluxes ratio. Although the $L_{\rm IR}$ of some separated galaxies does not meet the requirement of LIRGs ($10^{11}L_\odot$), we still include these sources in our sample.

Then we performed the photometry with the *IRAF* ellipse package. First, we fitted ellipse isophotes to *R*-band images. The center of the galaxies was determined by the contour map of *R*-band images. Many objects in our sample show the features of bars, rings, and interaction disturbance. For this reason, the ellipse isophotes were derived by allowing the position angle (PA), ellipticity $\left(e = \frac{a-b}{a}\right)$, and galaxy center to vary along the radius during the fitting process. Starting values of ellipticity and PA were determined by eye from the contour map of the galaxies in the *R* band. We derived a set of concentric elliptical isophotes that are extended from the

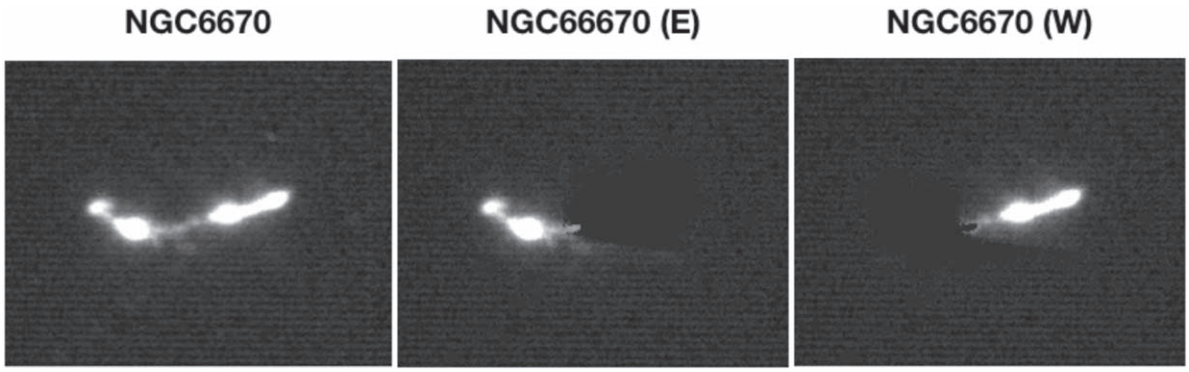

Figure 5. Example of interaction galaxy separation. The interacting galaxies with regions overlapped are separated by *Sextractor* (NGC 6670 in the *R* band).

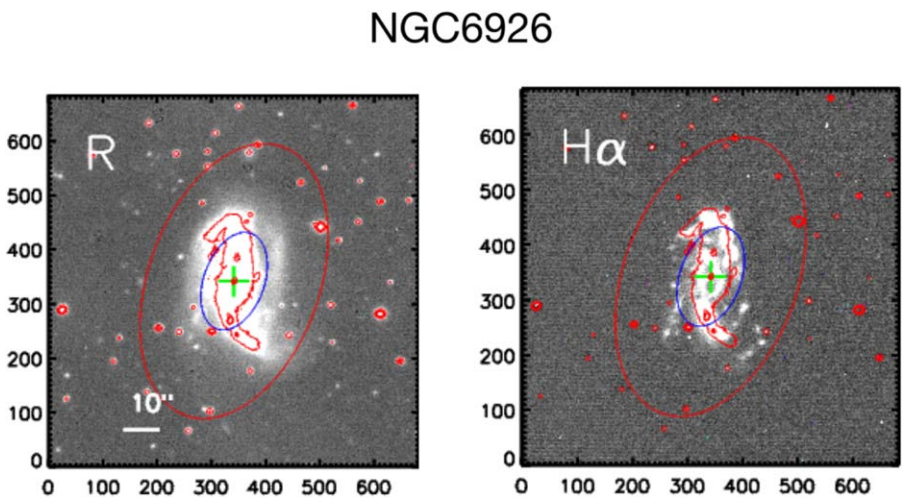

Figure 6. Example of galaxy boundary radius. The left panel is the *R*-band image, and the right panel is the continuum-subtracted Hα image. The red ellipse represents the boundary radius (radii *R*), the blue ellipse represents the R_e radius, the green cross represents the galaxy center, and the red contours are for the *R* band. The solid line on the *R*-band image represents 10″.

nuclear region to the outskirts of the galaxies. When the variation of the enclosed flux was close to zero among at least five isophotes, we used this radius as the boundary of the galaxy (radii *R*). We also get the half-light radius (R_e) at which the enclosed *R*-band fluxes reach half of the total.

The photometry of Hα was measured using the ellipse isophotes obtained from *R*-band images. Figure 6 shows the two ellipses for NGC 6926, which enclosed the total flux (red one) and half flux (blue one).

The *R*-band and continuum-subtracted Hα images are presented for each object in Appendix A (Figure 16).

3.3. Hα Flux Correction

The corrections for Hα flux include (1) Hα filter transmission; (2) [N II] emission; (3) both Galactic and internal galaxies extinctions.

Because some of the redshifted Hα lines may locate at the lower transmission part of the filter band, we applied transmission correction to the objects as suggested by Lei et al. (2018). A normalized transmission $T(\mathrm{H}\alpha)$ was used for the correction:

$$T(\mathrm{H}\alpha) = \frac{T'(\mathrm{H}\alpha)}{\int_{\lambda 1}^{\lambda 2} T'(\lambda) d\lambda \Big/ \mathrm{FWHM}},$$

where $T'(\lambda)$ presents the transmission curve, $T'(H_\alpha)$ is the direct transmission of redshifted Hα emission, the FWHM represents the width of the Hα filter curve at half of its peak value, $\lambda 1$ and $\lambda 2$ represent the beginning and end wavelengths of the transmission curve, respectively. The transmission-corrected Hα flux is obtained by dividing $T(\mathrm{H}\alpha)$. In addition, the flux in the *R* band also contains the Hα emission, which will result in underestimate for Hα flux in the process of continuum subtraction. Such loss (4%) was estimated by Lei et al. (2018) and corrected for our objects.

Wu et al. (1998b) performed a spectroscopic observation of 73 LIRGs and provided a ratio of [N II]/Hα for this sample. We took the mean value (0.55) of these LIRGs and then used it to correct the [N II] emission in our sample.

The Galactic extinction was corrected by using the Schlegel et al. (1998) map and the extinction curve from Fitzpatrick (1999). There are several methods for estimating the intrinsic extinction of Hα. Young et al. (1996) derived this correction from the [S III]/Hα ratio. Theios et al. (2016) assumed a correction of 1 mag based on the $L_{\mathrm{H}\alpha}$–SFR relation. The internal extinction in the work of Gavazzi et al. (2012) was performed by using the Balmer decrement. As there were no spectral emission lines that we can used for internal extinction correction, we adopted the MIR luminosity to estimate the intrinsic extinction of the Hα flux. Zhu et al. (2008) presented a correlation between *Spitzer* 24 μm MIR and extinction-corrected Hα luminosities for star-forming galaxies. By combing the Hα emission line and 24 μm measurements for

nearby galaxies, Kennicutt et al. (2009) got a similar relation and derived the formula. We chose their formula as

$$A(\mathrm{H}\alpha)(\mathrm{mag}) = 2.5\log\left[1 + \frac{0.020L(24)}{L(\mathrm{H}\alpha)_{\mathrm{obs}}}\right],$$

where $L(24)$ is the *Spitzer* MIR luminosity at 24 μm (here we adopted *IRAS* 25 μm instead) and the $L(\mathrm{H}\alpha)_{\mathrm{obs}}$ observed Hα luminosity without internal extinction correction.

The main errors of Hα fluxes include photometry and continuum subtraction. The photometric errors due to the Hα photon counting noise and background noise are typically smaller than 4%. The scaling factor of continuum subtraction is the dominant source of uncertainty. Even small uncertainties in scaling factor can result in large uncertainties in Hα flux with relatively weak Hα emission. We produced continuum-subtracted Hα images with a range of scaling factors. And then the accuracy of the scaling factor was estimated by the value at which the continuum-subtracted Hα images are clearly oversubtracted and undersubtracted. The typical errors in continuum subtraction is around 25% and in a few exceptional cases, this error reaches 70%. By the way, the errors of the internal extinction correction are mainly composed of two parts. One is the uncertainty of the extinction correction formula (typically 15%), and the other is the error of *IRAS* 25 μm fluxes (typically 5%).

4. Hα Imaging Results

In this section, we present the primary results of Hα imaging observations. Table 2, together with Figure 16, constitutes the main results of our observation.

4.1. Hα Catalog

The Hα photometry results of 158 galaxies are listed in Table 2. Both Hα Luminosity before and after internal extinction correction are given, as well as the ratio between Hα flux enclosed in R_e and that of the total galaxy.

Column (1): Source name;

Column (2): Type—the morphology and interaction type of the (U)LIRGs (a detailed description will be given in the next section);

Column (3): The $L(\mathrm{H}\alpha)_{\mathrm{obs}}$—the observed H$\alpha$ luminosity after correcting for transmission, [N II] emission, and Galactic extinction in units of erg s^{-1};

Column (4): The $L(\mathrm{H}\alpha)$—the Hα luminosity after correcting for internal extinction in units of erg s^{-1};

Column (5): Frac(Hα)—theratio between Hα flux enclosed inside R_e and the total;

Column (6): PA—the adopted position angles at galaxy boundaries (radii R);

Column (7): e—the adopted ellipticity at galaxy boundaries (radii R).

Figure 7 shows a comparison of the Hα emission fluxes measured by us with those of Young et al. (1996). The objects of Young et al. (1996) were measured without the correction of [N II] emission, internal galaxy extinction, and Galactic extinction. In the comparison, we complete the same steps as their work and give the resulting comparison. All objects show a good agreement around 0.24 dex.

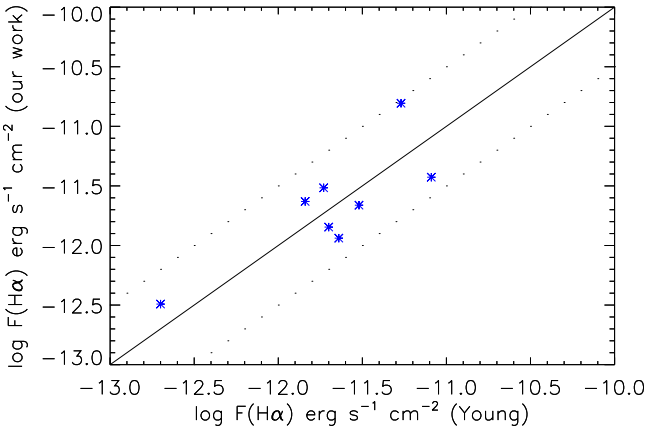

Figure 7. Comparison of Hα fluxes for galaxies in our work with those of Young et al. (1996).

4.2. Hα Images

Figure 16, in Appendix A, presents the R-band and continuum-subtracted Hα images for all 158 objects. These images were reduced by using the standard IRAF task. The WCS parameters in the FITS header were added using Astrometry.net. We calibrate the images by adding the flux calibration scale value to the imaging header as "scale." The count value can then be scaled to flux (erg cm^{-2} s^{-1}) by multiplying this value. This "scale" value also includes the correction for the Hα filter transmission and the 4% underestimate for the Hα flux. We did not make [N II] emission, Galactic, and internal galaxy extinction corrections for the "scale" value. These images are listed in order of object name, and the solid line in the R-band images represents 10″. All these images are available in FITS format.

5. Morphology Analysis

5.1. Morphology Classification

We divided the sample into several morphological classes in order to understand their role in the evolution of galaxies. We made our own morphological classification based on the R band as follows:

Spiral (S)—spiral galaxies with a symmetrical disk and showing no signs of tidal interaction;

Pre-Merger (PM)—two galaxies can be separated with asymmetrical disks or tidal tails, which could be the phase before merging;

Merger (M)—galaxies containing two nuclei with a tidal tail or the galaxies are disturbed severely, which is associated with most violent dynamical events;

Later Stage of Merger (LM)—single nucleus with a short, faint tidal tail, which may in the late stage of merger;

Elliptical Galaxy (E)—elliptical galaxies with an approximate ellipsoidal shape and without tidal interaction, which could be in final phase of merger;

Unknown (UN)—objects that cannot be classified by their morphology clearly.

Examples of different morphological classes are given in Figure 8. The classification was done independently by different people and a consistent classification was adopted after deliberated discussions. In our classification, the E-type occupies the smallest fraction (2.5%) among morphological types. The M-type occupies the largest fraction (39.2%). (U)

Table 2
The Hα Luminosity Information

(1) Name	(2) Type[a]	(3) $\log L(\mathrm{H}\alpha)_{\mathrm{obs}}$[b] (erg s^{-1} cm^{-2})	(4) $\log L(\mathrm{H}\alpha)$[c] (erg s^{-1} cm^{-2})	(5) Frac(Hα)[d]	(6) PA (deg)	(7) e
Arp220	M	41.76	43.20	0.69	20.00	0.10
CGCG 011-076	S	41.87	42.52	0.77	−82.57	0.38
CGCG 043-099	M	41.33	42.56	0.74	−64.31	0.15
CGCG 049-057	E^*	40.71	42.02	1.00	−14.80	0.07
CGCG 052-037	LM	42.09	42.59	0.75	52.07	0.27
CGCG 141-034	S^*	41.35	42.15	0.88	23.90	0.13
CGCG 142-034	M	41.47	42.13	0.63	74.97	0.64
CGCG 247-020	E	41.63	42.52	0.78	−55.31	0.02
CGCG 436-030	PM	42.00	42.90	0.82	32.29	0.19
CGCG 448-020	M	42.80	43.31	0.60	47.64	0.53
CGCG 453-062	LM^*	42.08	42.44	0.45	85.34	0.08
CGCG 465-012	M	42.17	42.50	0.85	66.00	0.04
CGCG 468-002	M^*	41.90	42.37	0.65	25.00	0.60
ESO 453-G005	M^*	41.83	42.35	0.71	−47.20	0.02
ESO 507-G070	M^*	41.61	42.42	0.86	−30.90	0.21
ESO 550-IG02(N)	PM	41.73	42.47	0.59	74.74	0.20
ESO 550-IG02(S)	PM	41.14	42.41	0.64	−64.05	0.45
ESO 557-G002	PM	42.05	42.48	0.83	−149.35	0.02
ESO 593-IG008	M	42.68	43.03	0.61	55.25	0.20
ESO 602-G025	M	41.92	42.55	0.81	9.36	0.69
ESO_467-G027	S	42.02	42.28	0.74	−52.76	0.34
IC 0214	M	42.32	42.67	0.52	5.00	0.10
IC 0860	S^*	40.31	42.15	0.63	−18.09	0.12
IC 1623A	M	42.84	43.13	0.67	−88.65	0.08
IC 2810	S	41.92	42.66	0.83	−40.78	0.52
IC 4280	S	42.16	42.41	0.80	−176.83	0.12
IC 5298	M	41.92	42.88	0.66	−21.05	0.03
IC 563	PM	41.99	42.34	0.67	53.57	0.67
IC 564	PM	41.96	42.33	0.54	−69.80	0.65
III Zw 035(N)	M^*	41.20	42.57	0.56	−18.90	0.45
III Zw 035(S)	M^*	41.20	42.57	0.36	−44.50	0.21
IRAS 03582+6012	M^*	42.27	42.69	0.66	−59.95	0.65
IRAS 04271+3849	LM	41.92	42.31	0.69	48.92	0.44
IRAS 05083+2441	LM	42.12	42.54	0.66	−22.06	0.44
IRAS 05129+5128	M	42.23	42.74	0.81	81.78	0.42
IRAS 05442+1732	LM	41.98	42.58	0.84	73.82	0.31
IRAS 17578-0400	LM^*	41.63	42.20	0.73	37.88	0.60
IRAS 18090+0130	M	42.26	42.73	0.56	−14.18	0.47
IRAS 19542+1110	E	41.83	43.20	0.76	−72.24	0.07
IRAS 20351+2521	M	42.04	42.70	0.96	10.15	0.09
IRAS 21101+5810	M	41.71	42.81	0.96	−110.33	0.22
IRAS 23436+5257	M	42.10	42.72	0.81	22.89	0.62
IRAS F01364-1042	E	41.31	42.69	0.88	−64.14	0.25
IRAS F02437+2122	E^*	40.99	42.22	0.94	71.27	0.36
IRAS F03217+4022	LM	41.17	42.15	0.56	72.34	0.28
IRAS F03359+1523	M	42.24	42.73	0.72	−74.38	0.73
IRAS F05187-1017	S^*	41.17	41.93	0.56	70.99	0.35
IRAS F05189-2524	E	42.24	43.49	0.64	−107.75	0.07
IRAS F06076-2139	M	41.80	42.68	0.63	−13.06	0.22
IRAS F08339+6517	LM	42.58	42.77	0.67	−153.41	0.05
IRAS F08572+3915	M	41.45	43.46	0.91	57.36	0.43
IRAS F09111-1007	PM	42.33	43.10	0.68	22.79	0.07
IRAS F10173+0828	S^*	41.56	42.84	0.75	76.02	0.54
IRAS F10565+2448	M	42.13	43.12	0.84	85.07	0.24
IRAS F12112+0305	M	42.09	43.26	0.76	54.77	0.22
IRAS F12224-0624	S^*	40.60	41.90	0.60	−32.78	0.16
IRAS F15250+3608	M	41.72	43.30	0.75	−56.70	0.03
IRAS F16164-0746	LM	41.24	42.40	1.00	74.64	0.47
IRAS F16399-0937	M^*	42.00	42.74	0.62	4.27	0.60
IRAS F16516-0948	M	42.37	42.57	0.50	20.00	0.10
IRAS F17132+5313	PM^*	42.39	43.02	0.87	0.56	0.41
IRAS F17138-1017	M	41.96	42.66	0.85	−1.53	0.43

Table 2
(Continued)

(1) Name	(2) Type[a]	(3) $\log L(\mathrm{H}\alpha)_{\mathrm{obs}}$[b] (erg s^{-1} cm^{-2})	(4) $\log L(\mathrm{H}\alpha)$[c] (erg s^{-1} cm^{-2})	(5) Frac(Hα)[d]	(6) PA (deg)	(7) e
IRAS F17207-0014	LM	42.11	43.21	0.59	56.78	0.16
IRAS F22491-1808	LM	42.23	43.22	0.65	78.85	0.24
IRAS F23365+3604	LM	42.03	43.28	0.77	−75.00	0.30
MCG+02-20-003	M	41.64	42.19	0.93	48.86	0.49
MCG+04-48-002	M	41.74	42.23	0.69	−60.56	0.30
MCG+05-06-036	S^*	41.77	42.68	0.78	−162.46	0.01
MCG+07-23-019	M	42.03	42.74	0.39	−84.19	0.10
MCG+08-11-002	M	41.33	42.33	0.81	69.80	0.28
MCG+08-18-013	PM	41.65	42.48	0.85	−45.20	0.27
MCG+12-02-001	M	42.39	42.83	0.63	56.78	0.26
MCG-02-01-051	PM	42.42	42.82	0.69	−49.62	0.50
MCG-02-01-052	PM	42.15	42.73	0.67	−25.88	0.60
MCG-02-33-098	M	41.91	42.53	0.90	−58.60	0.50
MCG-03-04-014	PM	42.30	42.85	0.81	20.84	0.25
MCG-03-34-064	E	42.51	42.93	0.82	−54.02	0.39
MCG01-60-022	LM	42.11	42.59	0.74	−87.54	0.27
Mrk231	M	43.29	43.99	0.79	−3.05	0.28
Mrk331	PM	42.18	42.72	0.88	−158.85	0.21
NGC 0317B	M	41.91	42.37	0.83	45.03	0.38
NGC 0838	LM	41.84	42.32	0.79	88.24	0.32
NGC 0958	PM	42.30	42.56	0.45	−3.49	0.53
NGC 0992	M	42.09	42.44	0.58	−11.33	0.29
NGC 1068	S	42.89	43.10	0.67	53.14	0.05
NGC 1275	M^*	42.94	43.14	0.74	80.00	0.10
NGC 1614	M	42.45	43.06	0.90	34.69	0.21
NGC 1797	LM	41.69	42.28	0.80	11.27	0.35
NGC 1961	M	42.35	42.50	0.46	−81.00	0.50
NGC 2146	M	42.14	42.46	0.75	48.34	0.62
NGC 23	S	42.13	42.44	0.72	12.80	0.28
NGC 232	PM	41.38	42.42	0.82	−5.94	0.23
NGC 2342	M	42.60	42.81	0.56	−79.46	0.29
NGC 2388	S	41.77	42.41	0.77	−74.63	0.01
NGC 2623	M	41.55	42.56	0.73	−34.12	0.46
NGC 3110	S^*	42.26	42.56	0.56	7.65	0.47
NGC 3221	S	41.66	42.15	0.70	10.05	0.71
NGC 34	M	41.65	42.68	0.76	−34.23	0.33
NGC 3690(E)	M	41.83	43.24	0.78	83.92	0.10
NGC 3690(W)	M	42.17	43.26	0.77	−64.14	0.10
NGC 4194	M	41.85	42.46	0.82	20.00	0.10
NGC 4418	S	40.34	42.47	0.53	−63.71	0.53
NGC 4922	M	41.38	42.68	0.83	25.52	0.33
NGC 5104	LM^*	41.82	42.34	0.60	11.41	0.48
NGC 5135	S	42.07	42.49	0.78	−18.82	0.23
NGC 5256	M	42.70	42.97	0.38	41.98	0.39
NGC 5257	PM	42.48	42.84	0.55	45.00	0.20
NGC 5258	PM	42.13	42.72	0.74	−41.19	0.42
NGC 5331	PM	42.06	42.66	0.95	58.42	0.50
NGC 5394	M	41.56	42.19	0.84	18.60	0.61
NGC 5395	M	41.92	42.31	0.44	4.50	0.60
NGC 5653	S	42.06	42.37	0.76	38.35	0.19
NGC 5734	LM	41.76	42.13	0.54	−45.11	0.11
NGC 5936	S^*	42.09	42.46	0.77	−24.30	0.30
NGC 5990	M	41.98	42.41	0.84	66.79	0.32
NGC 6052	M	42.66	42.76	0.49	−6.63	0.36
NGC 6090	M	42.72	43.03	0.82	−84.92	0.11
NGC 6240	M	42.57	43.18	0.79	−23.28	0.50
NGC 6286	PM	41.87	42.28	0.58	−22.67	0.04
NGC 6621	PM	42.13	42.55	0.84	40.00	0.30
NGC 6670(E)	M	42.03	42.74	0.68	57.03	0.38
NGC 6670(W)	M	42.06	42.74	0.49	−75.00	0.30
NGC 6701	S	42.04	42.38	0.68	37.64	0.04
NGC 6786	PM	42.38	42.84	0.65	−43.87	0.38

Table 2
(Continued)

(1) Name	(2) Type[a]	(3) $\log L(\mathrm{H}\alpha)_{\mathrm{obs}}$[b] (erg s^{-1} cm^{-2})	(4) $\log L(\mathrm{H}\alpha)$[c] (erg s^{-1} cm^{-2})	(5) Frac(Hα)[d]	(6) PA (deg)	(7) e
NGC 6907	PM	41.83	42.27	0.90	81.34	0.47
NGC 6926	M	42.42	42.67	0.52	−20.00	0.40
NGC 695	M	42.57	42.89	0.55	4.00	0.21
NGC 7469	M	42.81	43.15	0.84	−72.32	0.23
NGC 7591	PM	41.45	42.28	0.90	23.80	0.50
NGC 7592(E)	M	42.24	42.64	0.60	−13.00	0.40
NGC 7592(W)	M	41.83	42.52	0.78	−15.93	0.36
NGC 7674	PM	42.44	43.01	0.76	10.15	0.10
NGC 7679	LM	42.45	42.64	0.74	−175.80	0.06
NGC 7752	PM	42.15	42.41	0.73	−76.70	0.53
NGC 7753	PM	41.97	42.31	0.29	−48.87	0.38
NGC 7771	PM	41.89	42.46	0.72	−72.83	0.67
NGC 828	M	42.33	42.57	0.77	−75.00	0.30
NGC 877	PM	41.98	42.31	0.42	25.26	0.33
UGC 01385	S	41.93	42.39	0.92	25.03	0.20
UGC 03410	PM	41.74	42.14	0.74	58.57	0.74
UGC 04881	M	41.94	42.75	0.54	−56.23	0.58
UGC 08387	M	41.32	42.65	0.81	31.01	0.51
UGC 08739	PM	41.46	41.99	0.73	58.15	0.71
UGC 11041	S*	41.99	42.30	0.62	−46.16	0.33
UGC 12150	S	41.62	42.34	0.90	−44.58	0.12
UGC 1845	S	41.54	42.20	0.82	34.59	0.35
UGC 2238	M	41.64	42.25	0.95	14.44	0.38
UGC 2369	M	42.03	42.97	0.89	−86.15	0.27
UGC 2608	M	42.42	42.79	0.75	−62.01	0.24
UGC 2982	LM	42.17	42.42	0.59	75.09	0.42
UGC 3094	S	42.20	42.60	0.60	5.00	0.60
UGC 3351	PM	41.59	42.13	0.67	5.79	0.42
UGC 3608	M	42.39	42.72	0.74	−35.39	0.31
UGC 5101	M	41.81	42.92	0.73	−72.24	0.41
VII ZW 031	E*	42.45	43.06	0.74	34.00	0.10
VV250a	PM	42.21	43.05	0.82	61.24	0.49
VV340a	PM	42.19	42.59	0.36	−75.00	0.30
VV705	M	42.03	43.12	0.95	39.98	0.25

Notes.
[a] The morphology and interaction type of (U)LIRGs and the unknown objects is marked by *.
[b] The Hα luminosity after correcting for transmission, [N II] emission, and Galactic extinction.
[c] The Hα luminosity after correcting for internal extinction.
[d] The ratio between flux enclosed in R_e and total.

LIRGs in S-type, PM-type, and LM-type occupy the percentages of 10.8, 20.9, and 11.4, respectively. The UN occupies 15.2%. Figure 9 shows the distribution of morphological classes in histograms.

5.2. Infrared Luminosity

Figure 10 shows the distributions of L_{IR}. The black lines show the distribution for the whole sample. The distributions for other morphology types are also given in this figure (S: orange, PM: green, M: blue, LM: purple, and E: red). As can be seen, the S-type appears to be skewed toward smaller values, and none of them have L_{IR} larger than $10^{11.65}$ $L_{\odot}$, which is consistent with previous works (Wang et al. 2006; Lam et al. 2015; Larson et al. 2016).

The median L_{IR} of the PM-type, M-type, LM-type, and E-type morphologies is shown in each panel of Figure 10. And as the merging process advanced the objects had a tendency to have a relatively extended tail toward larger L_{IR}. Ishida (2004) showed the same result in their study of 56 LIRGs that the separation between merging galaxies decreases as IR luminosity increases.

5.3. Hα Luminosity and Concentration

In Figure 11, the histogram of Frac(Hα) is shown for each morphological type. It is clear that for most (U)LIRGs, the star forming is dominated by the central region with Frac (Hα) > 0.5. The S-type has a moderate concentration among all types with a median value of 0.77.

Frac(Hα) is also expected to be higher following the advancement of the merging process (Bryant & Scoville 1999; Hattori et al. 2004). Frac(Hα) of the PM-type is the minimum, and increases along the merging sequence from M- and LM- to E-type. The median value of Frac(Hα) is shown in each panel of Figure 11.

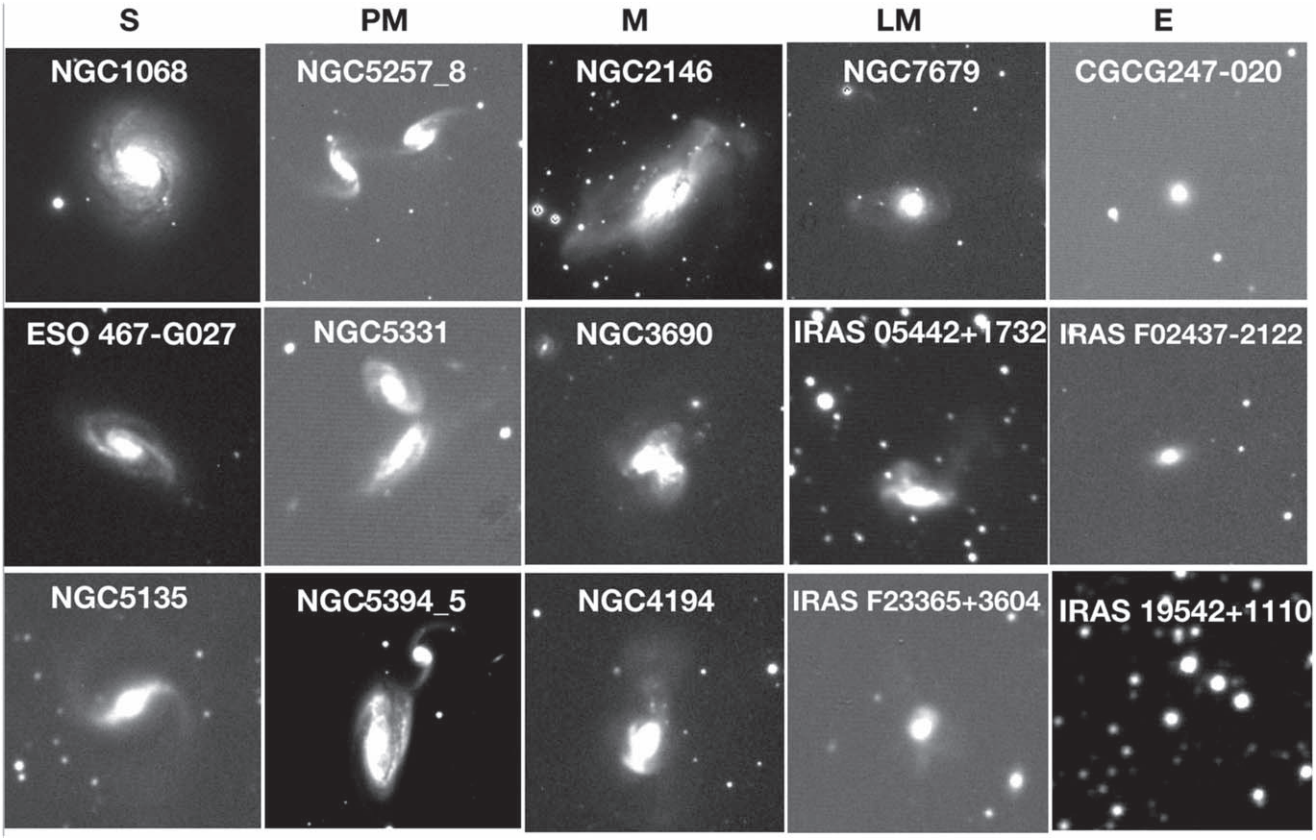

Figure 8. Example galaxies that are grouped into five morphological types: S: spiral galaxies; PM: galaxy in the predecessors of merger stage; M: galaxies in the most violent merger stage; LM: galaxies in late merger stage; E: elliptical galaxies. In all cases north is up and east is left.

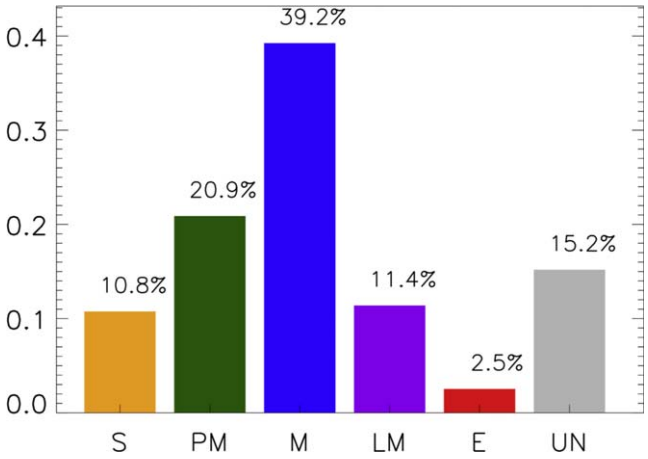

Figure 9. Distribution of morphology type: S (orange); PM (green), M (blue), LM (purple), E (red), and UN (gray).

5.4. Hα Profile

Figure 12 shows the profile for various morphology types. The 10 edge-on galaxies (S: 2; I: 6, M: 1, LM: 1) are not involved. In the direction of intensity, we normalize the profile with center intensity. In the direction along the galaxy's radii, we normalize the profile with galaxy boundary radii R. Then we combine the profiles according to their morphology types.

The PM-type is characterized by an exceptionally extended profile. The S-type also shows some extensions in the outer region. The PM-type galaxies may be dynamically young systems, which are predecessors for the advanced merger stage. On the other hand, the E-type galaxies that are relaxed from interaction without sign of interaction are the most compact ones. The M-type and LM-type are similar and have an intermediate profile among others.

By using the MIR emission of LIRGs, which can show the structures for different merger stages, Hwang et al. (1999) found that the peak-to-total flux ratios of LIRGs increase as projected separation of interacting galaxies becomes smaller. The profile as well as Frac(Hα) in our study are consistent with previous studies where (U)LIRGs tend to have more concentrated star formation distribution as the merging process advances (Bryant & Scoville 1999; Hattori et al. 2004).

5.5. Infrared Color

The infrared colors have been interpreted by various models (Helou 1986; Sekiguchi 1987). A cool component temperature ($20K$) is used to represent the emission from dust in infrared cirrus heated by older stellar population and peaks at $\lambda \gtrsim 100$–$200\,\mu$m. A warmer component temperature ($30 \sim 60$ K) represents the starburst in galaxies and peaks near $60\,\mu$m. And an even warmer component peaking around $25\,\mu$m represents the dust emission heated by AGN.

The distributions of IR-color ($\log(f_{25}/f_{60})$ and $\log(f_{60}/f_{100})$) are shown in Figure 13. The E-type has a warmer f_{25}/f_{60}, which may indicate they host an AGN. NGC 1068, a spiral galaxy, which also has warmer f_{25}/f_{60} (-0.35), is a well-known Seyfert2 galaxy. The rest objects do not have a clear tendency in f_{25}/f_{60}. In addition, (U)LIRGs tend to have warmer $\log(f_{60}/f_{100})$ as the merging process advances. The median

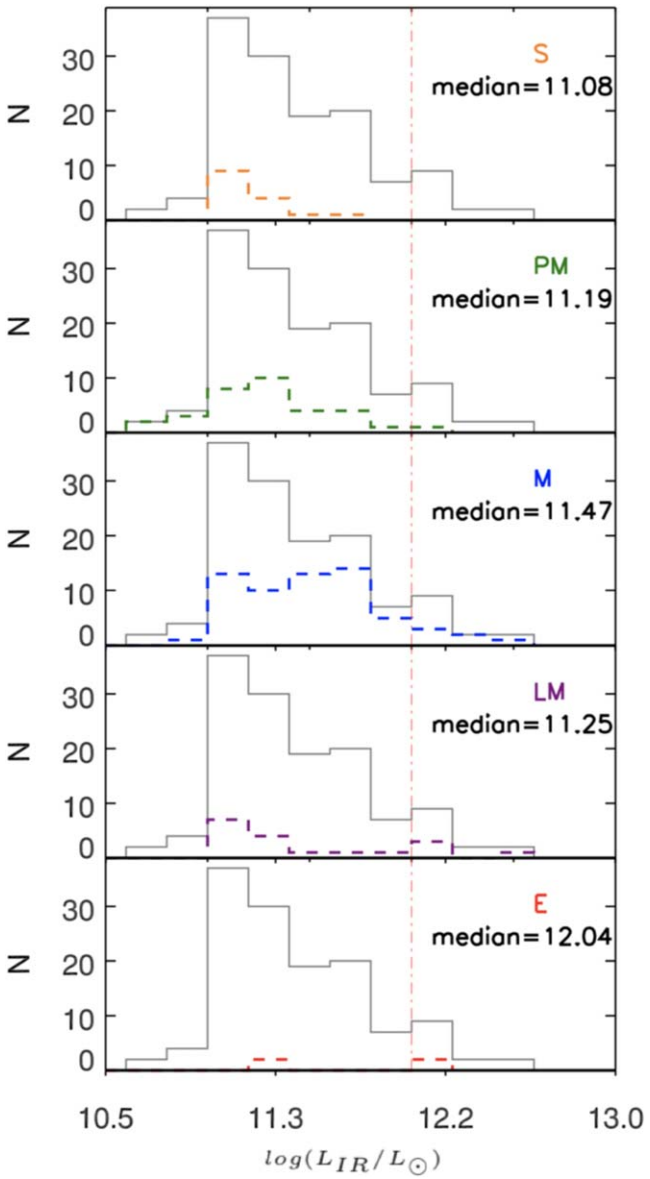

Figure 10. L_{IR} distributions of different morphology types. The boundaries of LIRGs and ULIRGs are shown with a vertical line (red dotted–dashed line). Colors are the same as those in previous figures, and the black lines show the distribution for the whole sample. The median value of L_{IR} for each type is also shown in the upper right corner of each panel.

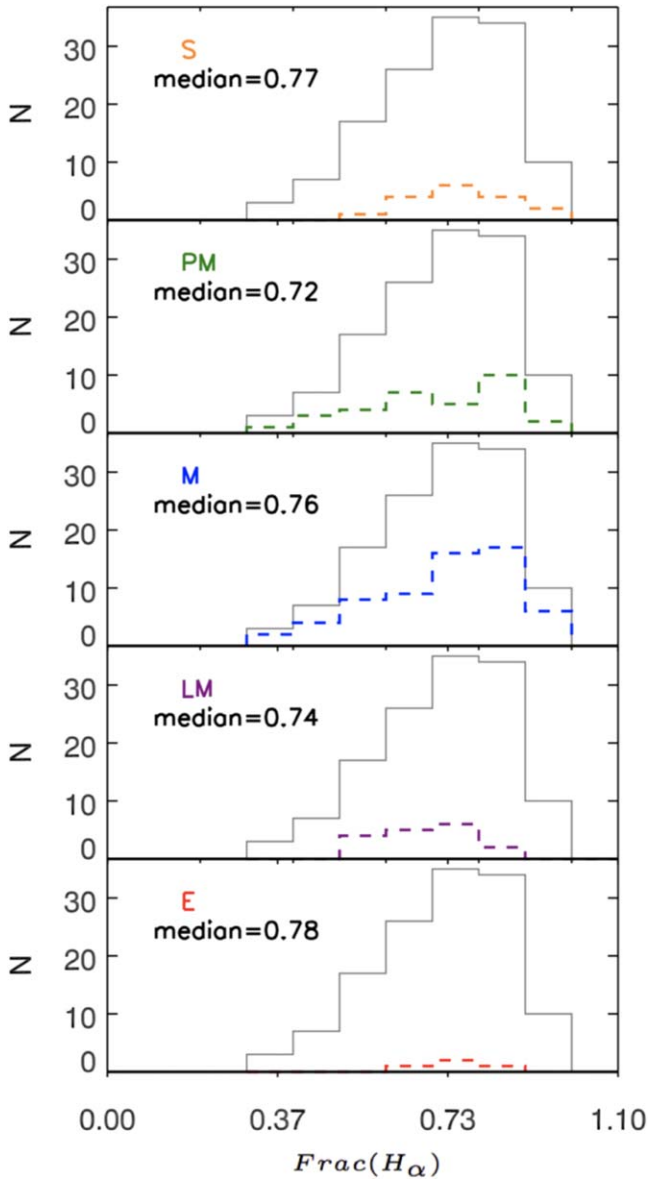

Figure 11. Distribution of Frac(Hα). Colors are the same as those in previous figures. The median value of Frac(Hα) for each type is also shown in the upper left corner of each panel.

values of both $\log(f_{60}/f_{100})$ and $\log(f_{25}/f_{60})$ are also shown in each panel of Figure 13.

6. Discussion

6.1. Importance of a Complete Hα Imaging Survey

The GOALS sample has become a "reference sample" for studying the properties of (U)LIRGs in the local universe. Extensive multiwavelength (radio to X-ray) imaging and spectroscopic data have been obtained for different subsamples of GOALS. Although the Balmer Hα emission line is a good indicator of star formation rate and there are some Hα imaging observations containing sources belong to the GOALS sample, until now, there have been no complete Hα observation data for this "reference sample."

In this work, we performed an Hα survey for a complete GOALS subsample with decl. $\geqslant -30°$. After continuum subtraction, we obtained 148 pure Hα emission images, which can provide the star formation distribution for this GOALS subsample. We also provide relatively complete Hα photometric data for the GOALS subsample for the first time. In summary, this survey provides an imaging and photometry component that is a useful data addition to the GOALS data archive, and is helpful in revealing the formation and evolution of (U)LIRGs.

6.2. Comparison with Other Morphological Classifications

Though there are many previous works focusing on morphological classifications (e.g., Haan et al. 2011; Kim et al. 2013 and Larson et al. 2016), their data do not completely cover objects in this work, and the classification results cannot be directly used. Here we do not use the same classification criteria as they do. Previous studies of LIRG morphology either

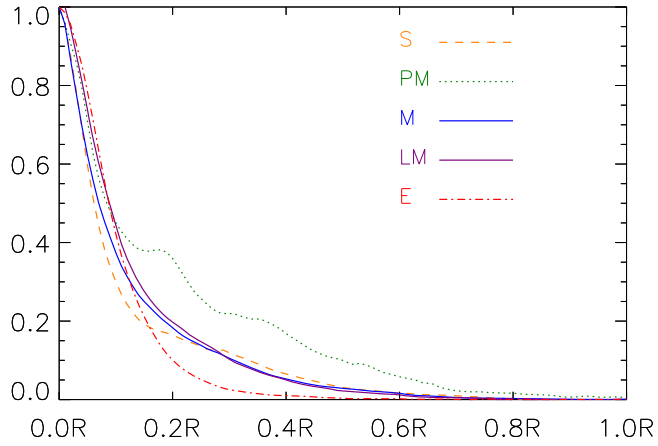

Figure 12. Isophotal shape of different morphology types. The orange dashed line represents the S-type, the green dotted line represents the PM-type, the blue solid line represents the M-type, the purple dotted–dotted–dashed line represents the LM-type, and the red dotted–dashed line represents the E-type. The horizontal coordinate is scaled with galaxy boundaries (R).

relied on *HST* higher-resolution ($\sim 0\farcs1$) imaging (Larson et al. 2016) or mainly focused on merger stages (Kim et al. 2013 and Larson et al. 2016). As such, there are no distinctions between spirals and ellipticals in the classification of single galaxies in Larson et al.'s (2016) and Kim et al.'s (2013) work. Considering these factors, as well as intending to distinguish the merger stage clearly, we adopt a simple approach focusing on the classification for the most important merger stages.

To ensure the reliability of morphology classification in this work, we compare our results (J19) to that of Larson et al. (2016, hereafter L16) and Kim et al. (2013, hereafter K13) in Figures 14 and 15 with a method provided by Larson et al. (2016). It should be noted that some merger stages, like minor merger (m) in L16, have no suitable analogs in our works. Moreover, because of different criteria for classification, as well as the difference in division of stages, there will be cases where one merger stage corresponds to multiple adjacent stages. For example, the merger stage M in our work corresponds to M3 and M4 in L16, and merger stage M4 in L16 corresponds to M and LM in our work.

In Figures 14 and 15, we mark the cells as green when the corresponding merger stages agree between two works. The classifications that are shifted by only one stage to an earlier or later stage are marked as yellow. Considering the morphology classification focuses on different characteristics, we treat this case as a consistent result. When the classifications differ by more than one stage, they are marked as red. There is a total of 63 objects that are included both in our work and L16. But 10 of them do not have a very certain classification either in our work (UN) or in L16 (ambiguities), and 4 of them are classified as a minor merger (m) in L16. Finally, there are a total of 49 objects in the comparison. It can be seen from Figure 15 that our classification agrees fairly well with those of L16 as 79.5% of objects have a very consistent classification (green) and 12.2% objects have a slight change (yellow). And there are still four objects that require a change greater than a single stage. Overall, our classifications are very consistent with that of L16. The four objects that require a change greater than a single stage are described in Appendix B. Sixty-one objects in our sample were also previously classified by K13 (Figure 14). Seven of them do not have a very certain classification in our work, and finally there are 54 objects in the comparison. The result of Figure 14 also shows that our classifications are consistent with that of K13 (92.6% are roughly the same: 46.3% objects have a very consistent classification; 46.3% objects have a slight change between our work and K13). The four objects that require a change greater than a single stage are described in Appendix B. The reason why a few objects differ in our classification with that of L16 or K13 is due to different resolutions of image and subjective factors. Finally, in order to maintain the consistency of our sample, we do not change our classification during the fellow analysis.

6.3. Isolated Spiral LIRGs

In our study, the local (U)LIRGs are dominated by a merging system and the S-type only occupies 10.8% among all types. Meanwhile, in Zheng et al.'s (2004) work, ∼36% of LIRGs with a redshift between 0.4 and 1.0 are classified as normal disk galaxies. Such a fraction is about three times the fraction in our local sample. The work of Melbourne et al. (2005) confirmed a decrease in the fraction of spiral galaxies in LIRGs from the higher redshift (∼1) to lower redshift.

As can be seen in Figure 10, the $L_{\rm IR}$ of spirals galaxies in our sample are no more than $10^{11.65}L_{\odot}$, which is consistent with previous works. Wang et al. (2006) also found that none of their spiral LIRGs have $L_{\rm IR}$ higher than $10^{11.6}L_{\odot}$. Both our and Wang et al. (2006)'s results suggest that the infrared luminosity of all the local S-type LIRGs are much lower than the boundary of ULIRGs ($L_{\rm IR} = 10^{12}L_{\odot}$). And in Lam et al. (2015)'s work, the spiral galaxies also tend to have lower $L_{\rm IR}$. Larson et al. (2016) presented an analysis of morphologies for 65 LIRGs in the GOALS sample. They found that the sources with $\log(L_{\rm IR}/L_{\odot}) \geqslant 10^{11.5}$ are dominated by major mergers between gas-rich spirals, and all ULIRGs are late-stage mergers. All of these results mean that the spiral LIRGs tend to have lower $L_{\rm IR}$ than those in merging systems in the local universe. The objects in S-type also have a moderate concentration of star-forming distribution in our sources. It seems that in the local universe, the galaxies have less gas than their counterparts at intermediate redshift. And without interaction, such types of galaxies cannot enhance the extreme starburst. At intermediate redshift, the $L_{\rm IR}$ of normal disk galaxies could be higher because of more gas and correspondingly more extensive disk star formation (Reddy et al. 2006). The decrease of disk gas could be one of the keys to explaining the decrease in the fraction of spiral galaxies in LIRGs from intermediate redshift to the local universe.

6.4. Merging Sequence

As normal spiral galaxies cannot reach a higher $L_{\rm IR}$, a merger/interacting process is needed to induce an extreme nuclear starburst. Here we explore the possible merging sequence according to our classification.

When two gas-rich spiral galaxies start their interaction, the tidal torques begin to lead an inflow of gas from the outer region to the central region. At this stage (PM-type), star formation occurs in both the nuclear and outer regions. The objects also tend to show a relatively low concentration of Hα (Figure 11) and a more extended Hα profile (Figure 12) with lower $L_{\rm IR}$ and colder IR-color. It is consistent with the evolutionary sequence described by Hattori et al. (2004). In their study, the objects in the early stage of interaction have a significant star formation contribution from the outer region.

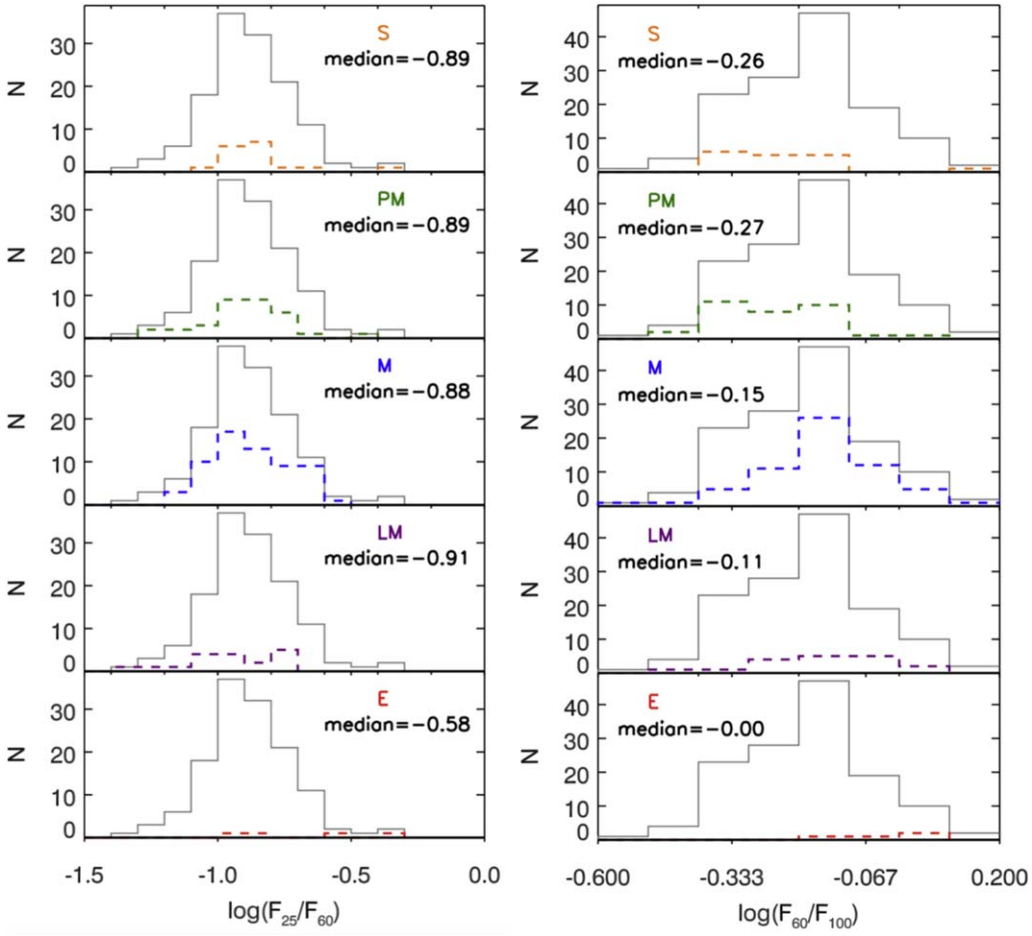

Figure 13. IR-color of different morphology types. Colors are the same as those in previous figures. The median value of IR-color for each type is also shown in each panel.

J19 \ K13	0	1	2	3	4	5	6
S	0	1					
PM	1	4	6				
M	4		10	6	6	8	
LM						4	1

Figure 14. Morphology comparison between this work (J19) and Kim et al. (2016, K13).

J19 \ L16	s	M1	M2	M3	M4	M5
S	2	1				
PM	1	5	10			
M	1		4	11	8	
LM	2			1	0	0
E	1			1		1

Figure 15. Morphology comparison between this work (J19) and Larson et al. (2016, L16).

Scoville (2001) showed that the interaction/merging increases the cloud–cloud collision that leads to a transport of molecular gas from the interstellar medium (ISM) to the nuclear region and triggers the starburst in the overlap region of galaxy disks.

As the merging process advances (M-type and LM-type), the two nuclei of the galaxies become closer. The gas continues to fall into the galaxy center and fuels the intense star formation activity. As a result, the star formation activities become more active and begin to concentrate toward the galaxy center. The results of previous section indicate that these objects in this stage have a more concentrated star formation region, higher L_{IR}, and a warmer dust temperature (larger f_{60}/f_{100}), which is caused by more intensive star formation activity. Wu et al. (1998b) showed the same result where both infrared luminosity and Hα equivalent width increase as galaxy–galaxy nuclear separation decreases. In the work of Lutz (1992) and Hattori et al. (2004), they both showed a warmer IR-color in this later merging stage. Many works also showed that in the later merging stage, the distribution of star formation gradually concentrated toward the center (Mihos & Bothun 1998; Hwang et al. 1999; Xu et al. 2000; Hattori et al. 2004). All this evidence indicates an intense nuclear starburst in this later merging stage.

In the last stage (E-type), the objects need to take some time to relax and move toward an elliptical morphology. They not only show the most concentrated distribution of the star

formation region and the highest L_{IR} and warmest f_{60}/f_{100} color but also have a statistically warmer f_{25}/f_{60} color. This means E-type may have strong and concentrated star formation activities as well as an AGN in their galaxy center (Zheng et al. 1999). It is a stage of coexistence of both star formation and AGN. This result is consistent with classical evolution from (U)LIRGs to QSOs.

In brief, this work shows that as the merging process advances from PM-, M-, LM- to E-type, the objects tend to present higher L_{IR}, more concentrated star formation, and warmer IR-color. All these properties support the evolutionary sequence in the (U)LIRGs of many former works (Sanders et al. 1988; Barnes & Hernquist 1992; Bryant & Scoville 1999; Hopkins et al. 2008; Jin et al. 2018).

7. Summary

In this paper, we have presented an Hα imaging observation for a complete subsample for GOALS with decl. $\geqslant -30°$. The observation was carried out using the 2.16 m telescope at the Xinglong Station of the National Astronomical Observatories, CAS, during the years 2006 to 2009. The data presented here are so far the most complete Hα imaging survey of the GOALS sample. For many of these objects, this paper presents the first imaging data and photometry of Hα emission.

(1) A total of 148 (U)LIRGs were observed during the Hα imaging survey. Given that there are 10 galaxy systems, our sample contains 158 galaxies. The subsequent data reduction mainly contains sky background, continuum subtraction, flux calibration, photometry, and the correction of [N II] emission, filter transmission, galactic extinction, and internal extinction. Finally, we obtained the Hα images (Figure 16) and luminosity catalog (Table 2) for this sample.

(2) We have visually classified our sample using a simplified classification that includes Spiral (S), Pre-Merger (PM), Merger (M), Later Stage of Merger (LM), and Elliptical (E). After comparing our classification with previous works, we find that our classification is consistent with those of others.

(3) The fraction of spiral galaxies is lower in LIRGs compare to their counterparts in higher redshift. The lower L_{IR} in local spiral galaxies also indicate that interaction between galaxies is needed to induce an extreme L_{IR} in the local universe.

(4) We also found that the advanced merging objects tend to have a concentrated star formation distribution, higher L_{IR}, and warmer far-IR-color. All of these results are consistent with the model of the merger that drives gas inward toward the nucleus and the star formation activity that will be concentrated and enhanced as the merging process advances.

We are grateful to the referee for the careful reading of the paper and useful comments and suggestions. This project is supported by National Key R&D Program of China (No. 2017YFA0402704), and the National Natural Science Foundation of China (grant Nos. 11733006, U1831119). The authors acknowledge the hard work of observation assistance for the 2.16 m telescope: Hong-Bin Li, Jia-Ming Ai, Junjun Jia, and Feng Xiao. This work was partially supported by the Open Project Program of the Key Laboratory of Optical Astronomy, National Astronomical Observatories, Chinese Academy of Sciences. This research has made use of the NASA/IPAC Infrared Science Archive, which is operated by the Jet Propulsion Laboratory, California Institute of Technology, under contract with the National Aeronautics and Space Administration. This work also used the published data from the Pan-STARRS1 Surveys (PS1).

Appendix A
R and Hα Images

We also show the *R*-band and continuum-subtracted Hα images (Figure 16) for each object in this appendix, in order of object name. The solid line on the *R*-band images represents 10″, and the object name is noted at the top of the images.

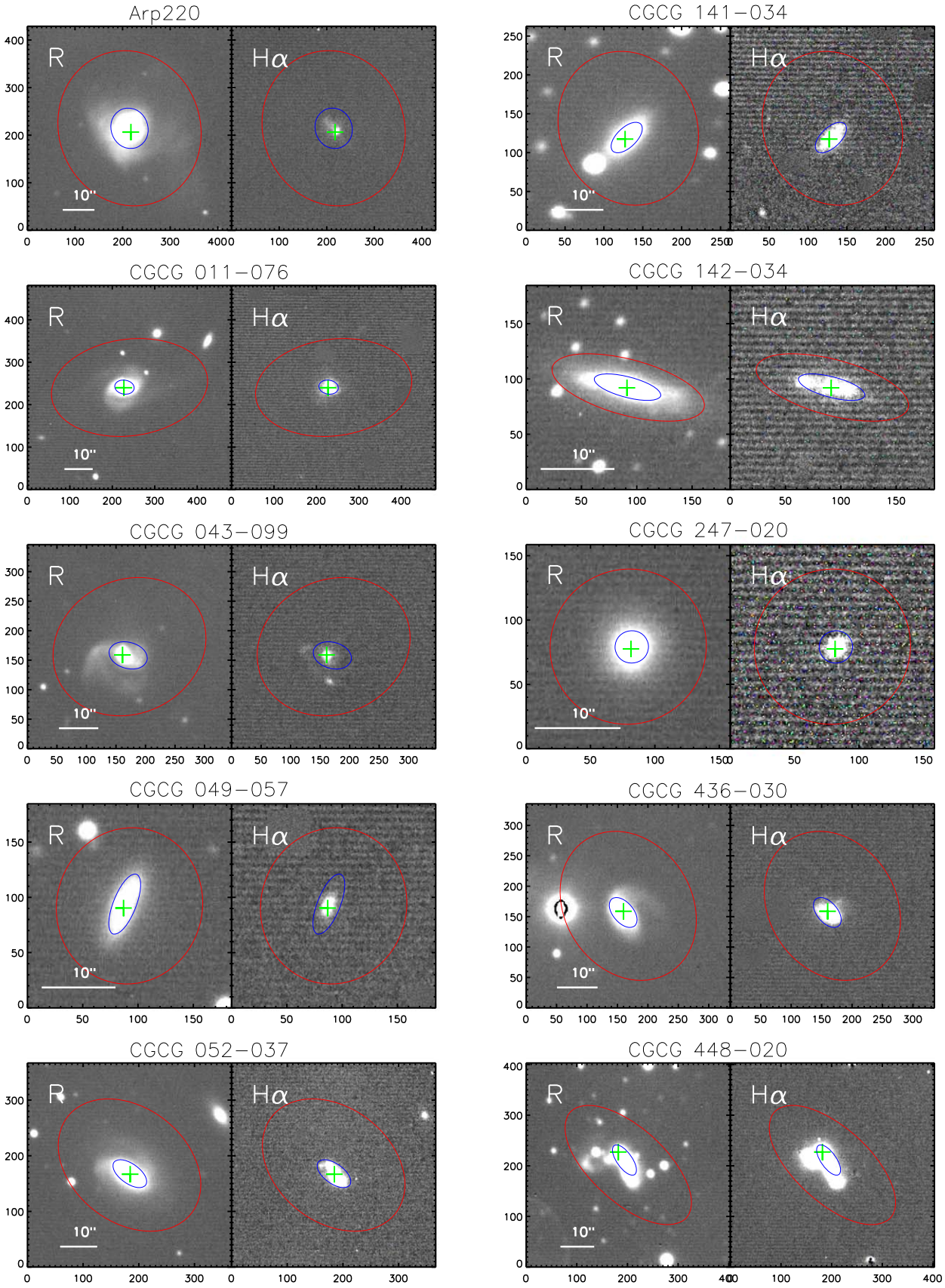

Figure 16. *R*-band image (left) and continuum-subtracted Hα image (right). The images are listed in order of object name. The solid line on the *R*-band images represents 10″. The other symbols on the *R*-band and continuum-subtracted Hα images are the same as in Figure 4. The object name is noted at the top of the images.

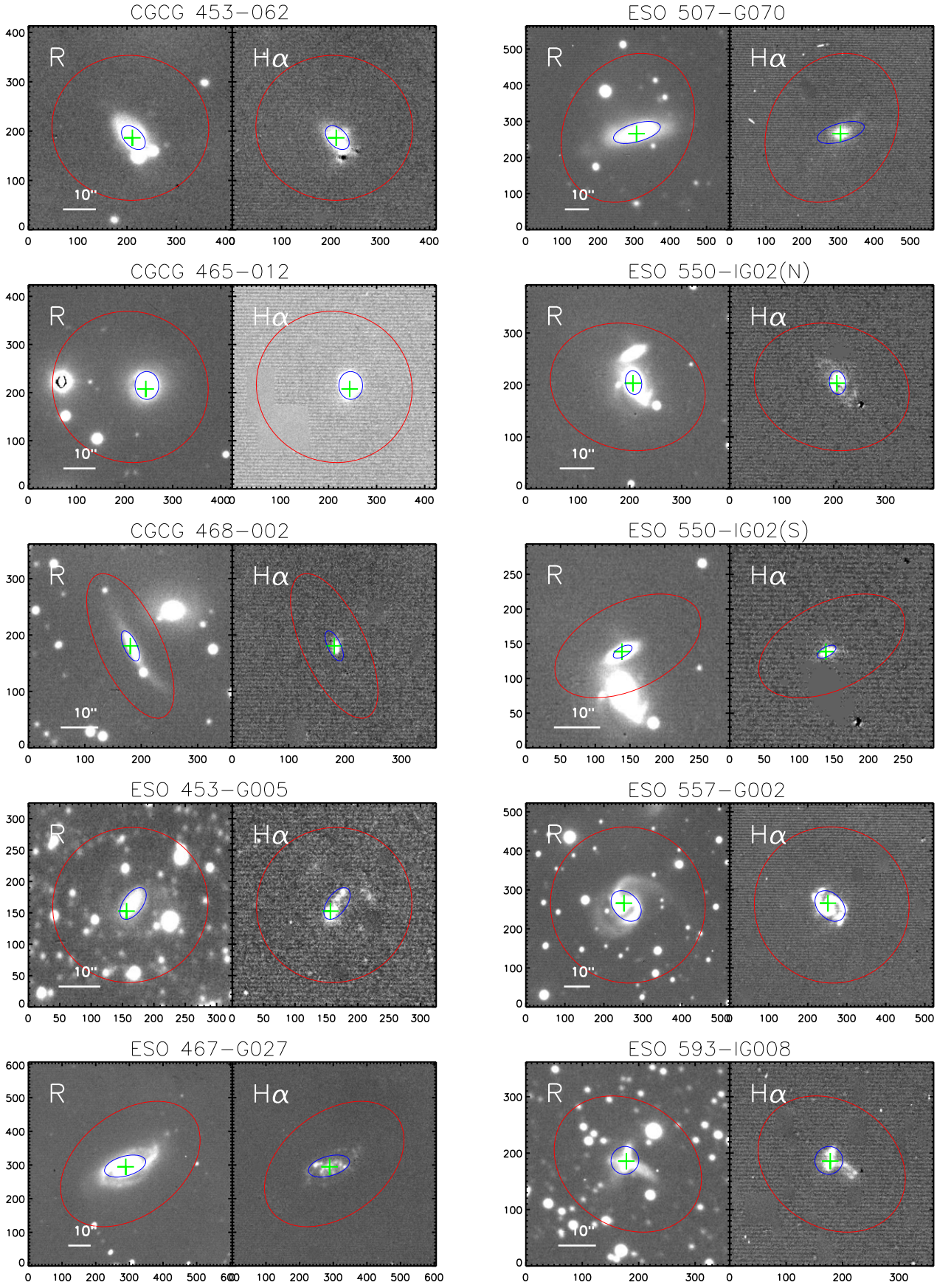

Figure 16. (Continued.)

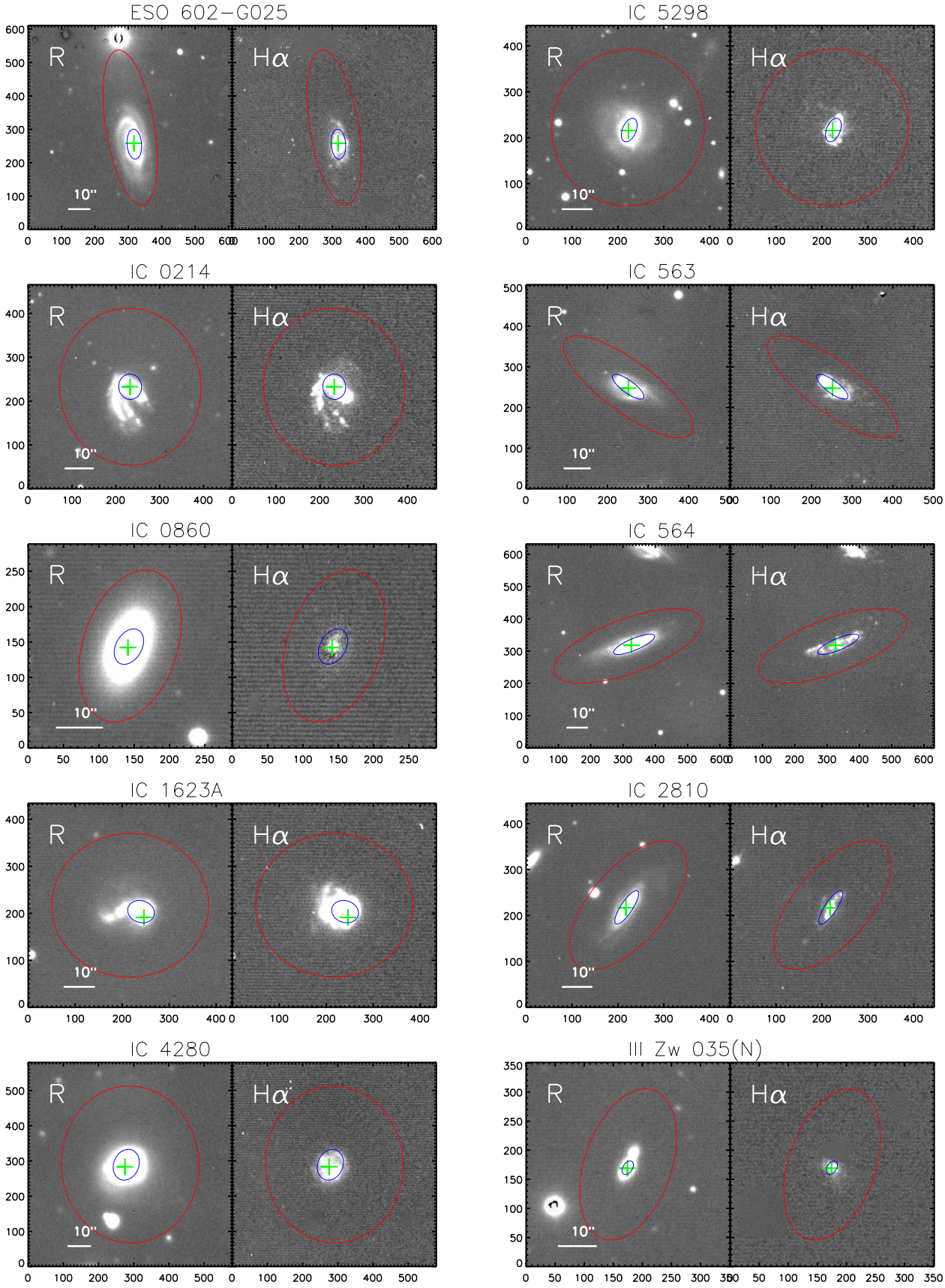

Figure 16. (Continued.)

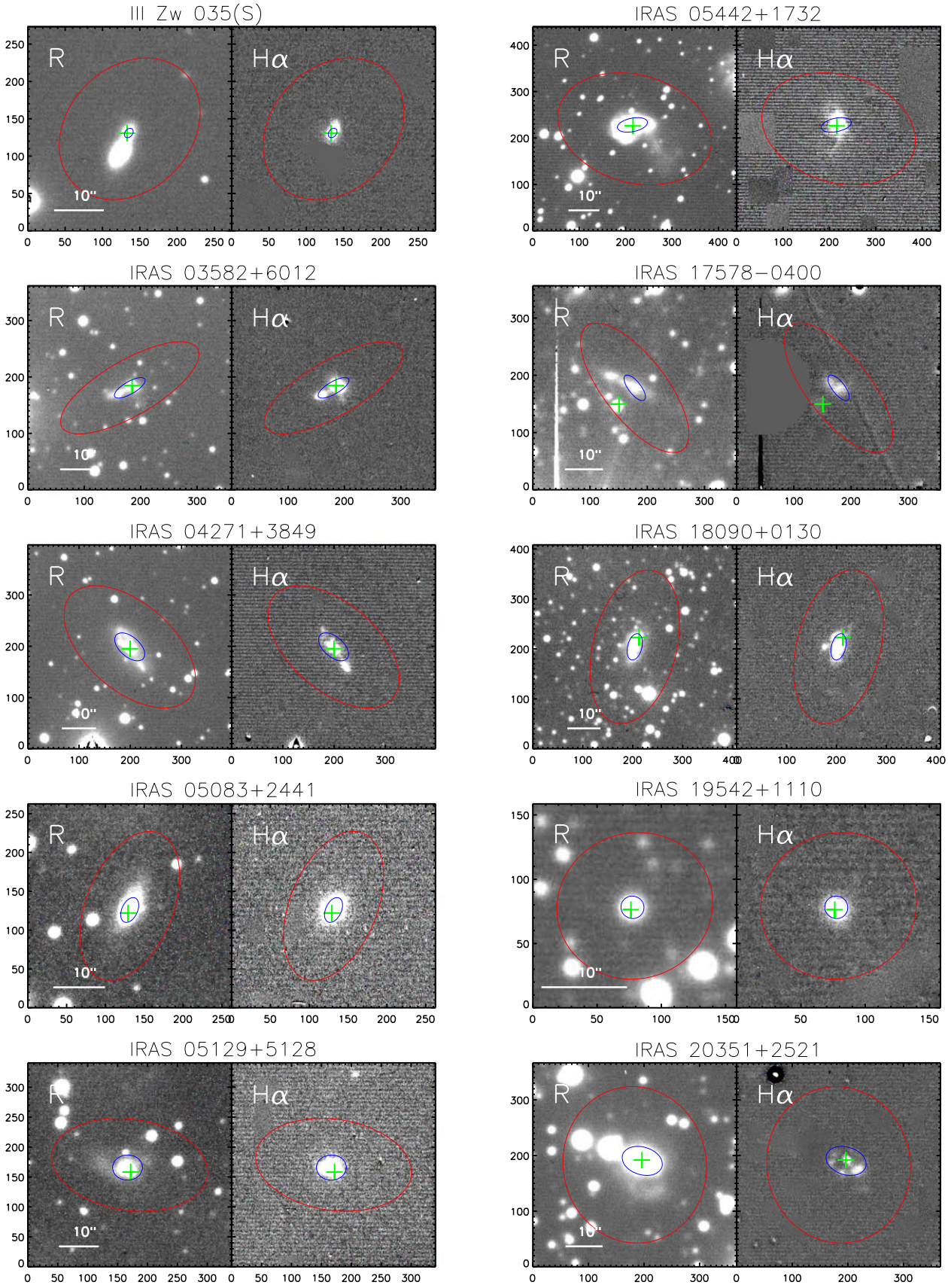

Figure 16. (Continued.)

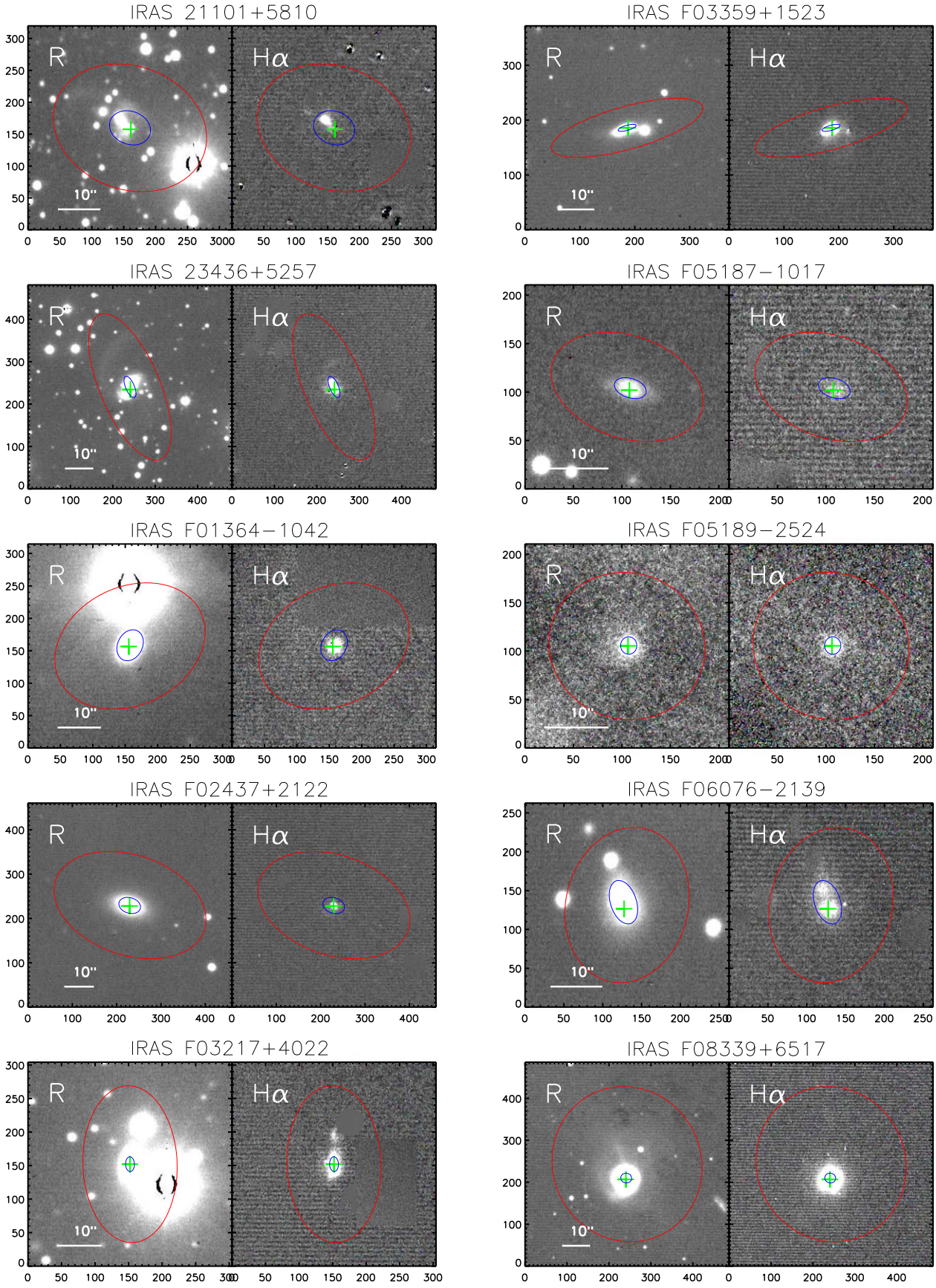

Figure 16. (Continued.)

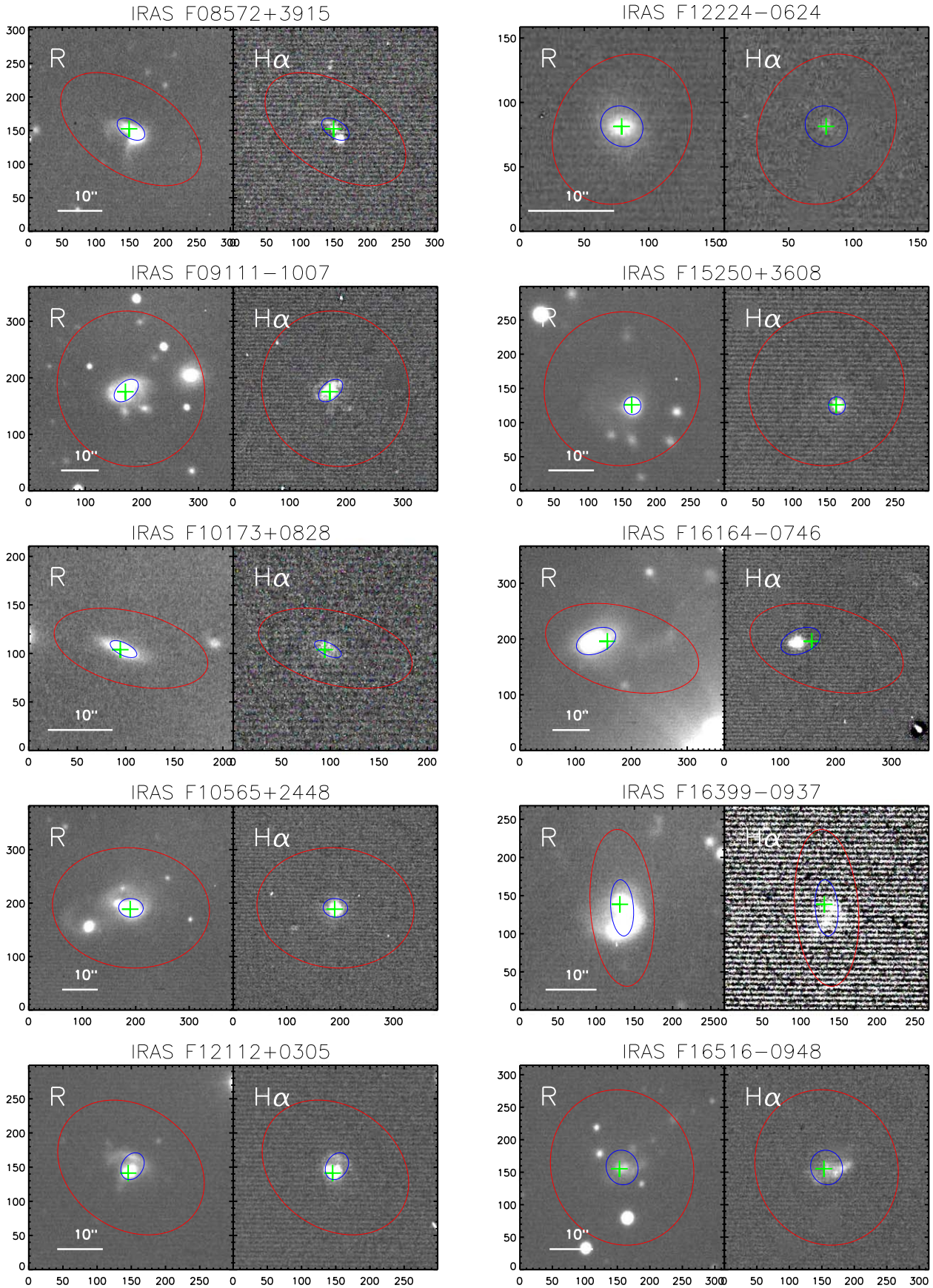

Figure 16. (Continued.)

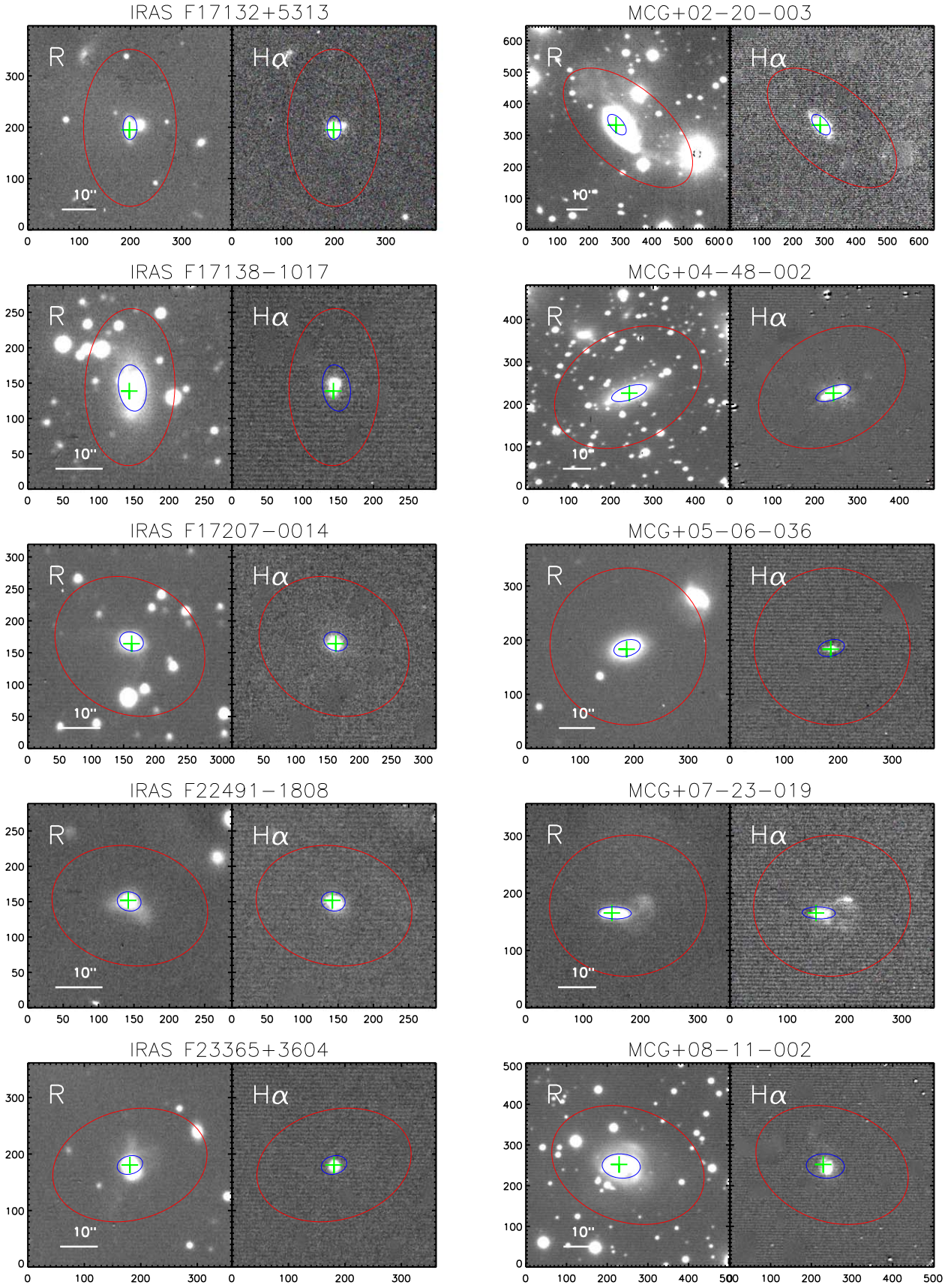

Figure 16. (Continued.)

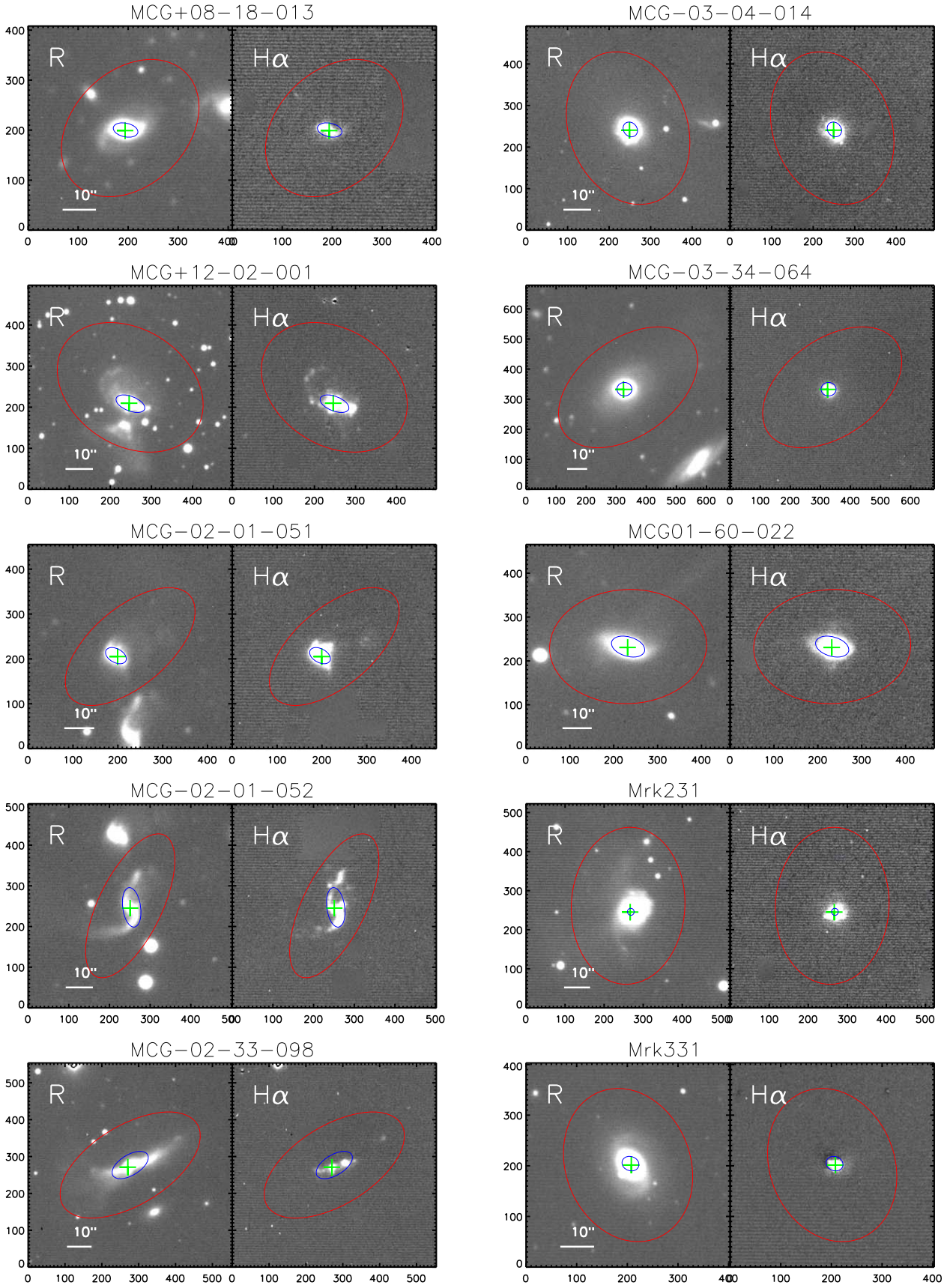

Figure 16. (Continued.)

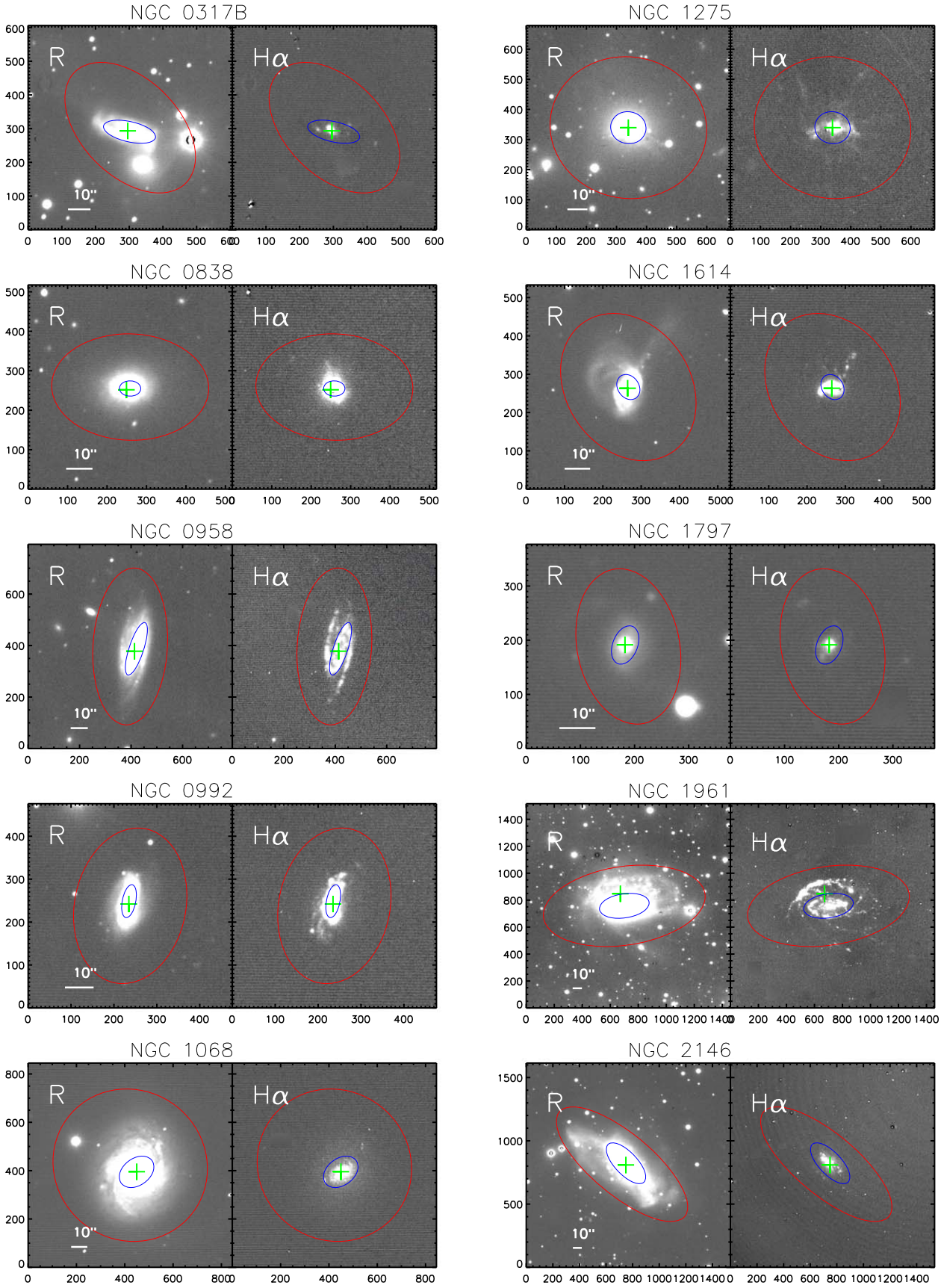

Figure 16. (Continued.)

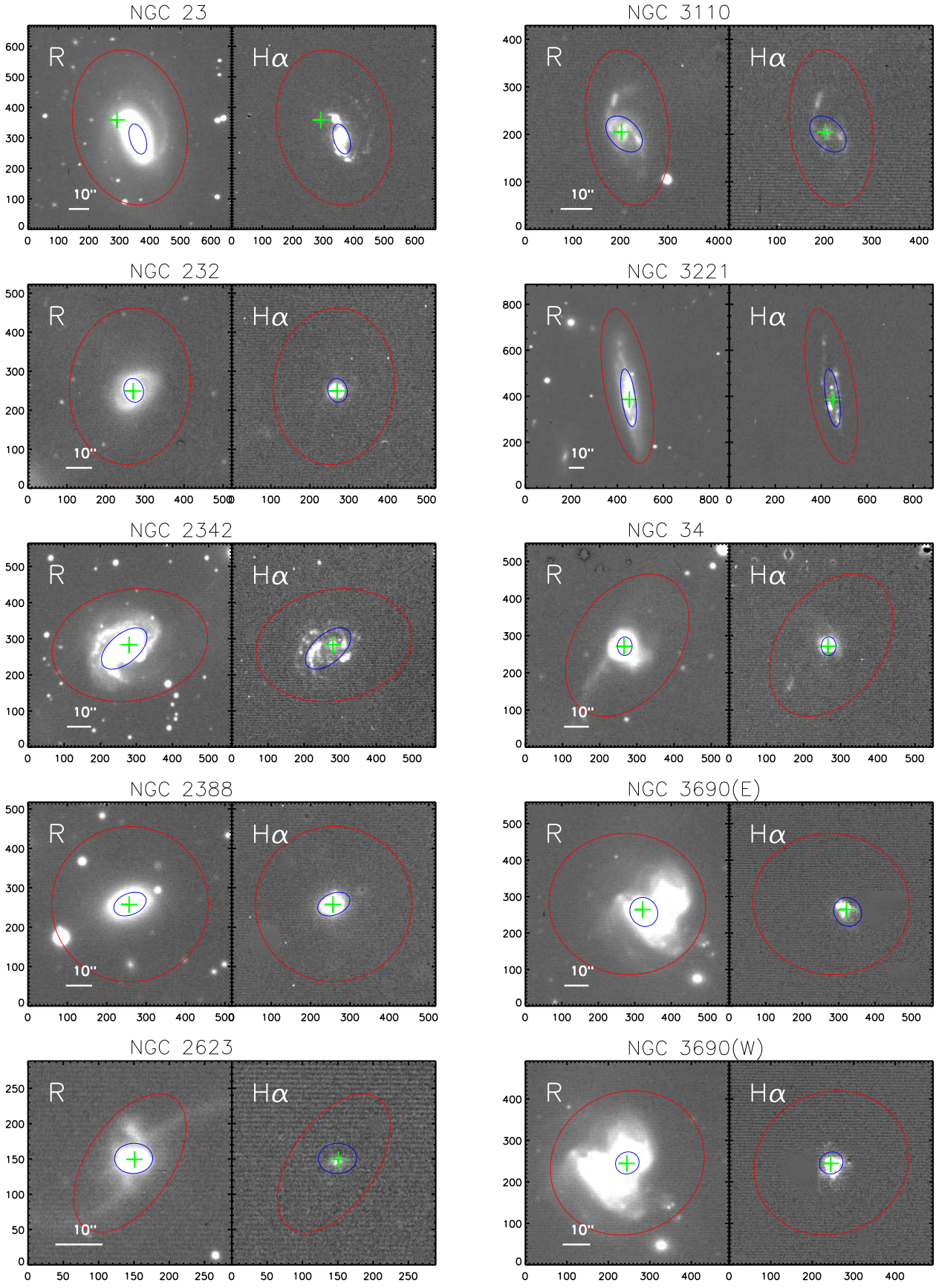

Figure 16. (Continued.)

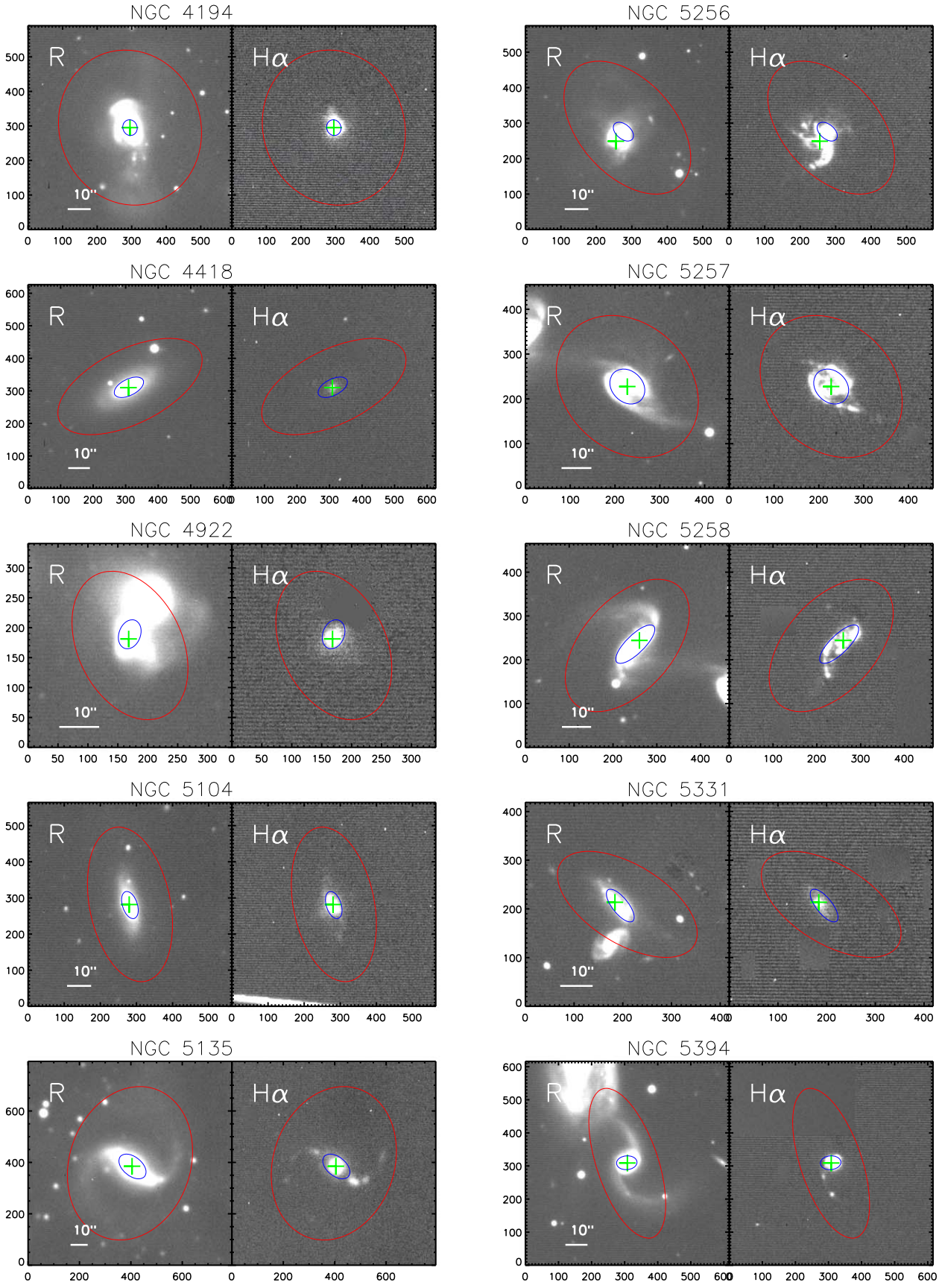

Figure 16. (Continued.)

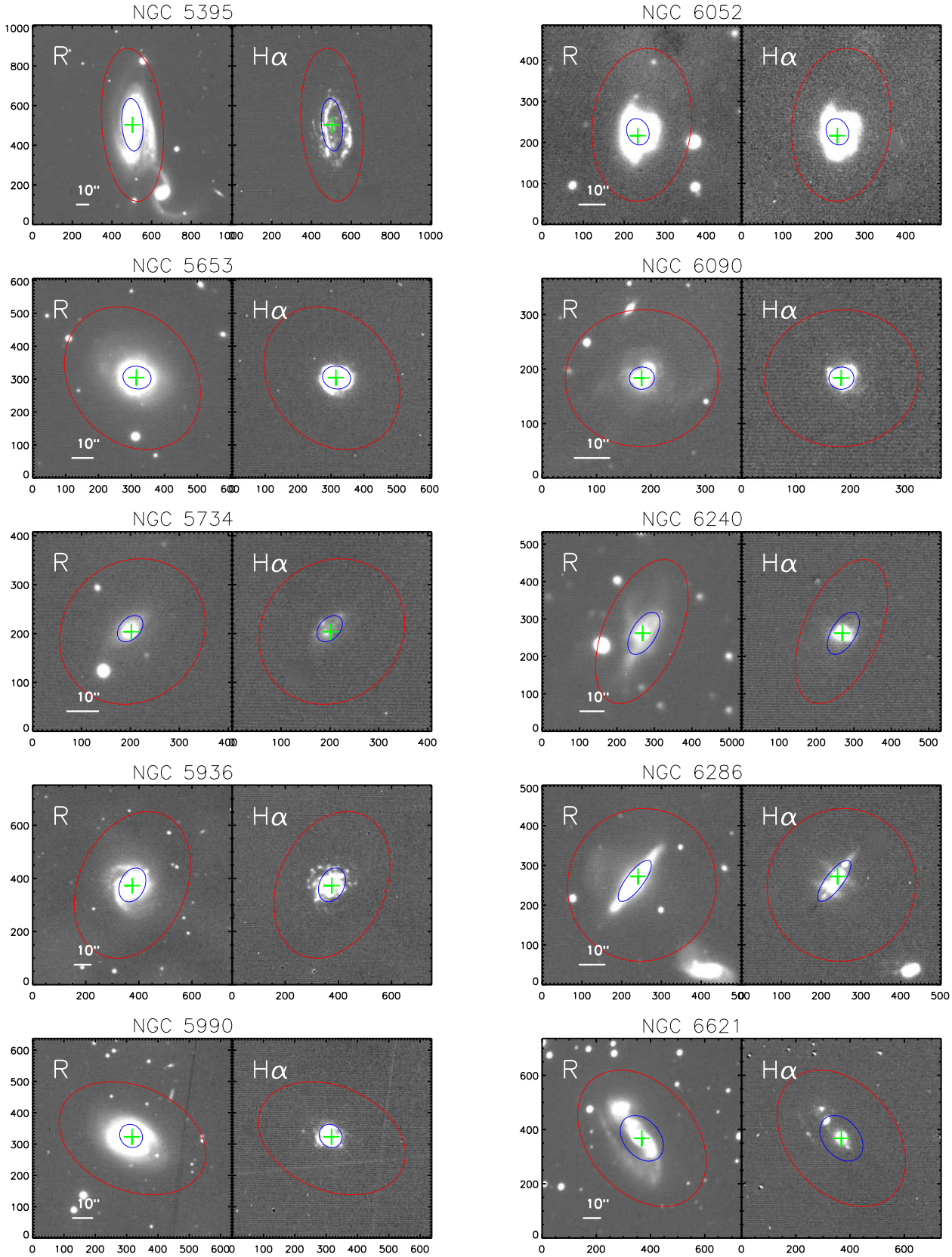

Figure 16. (Continued.)

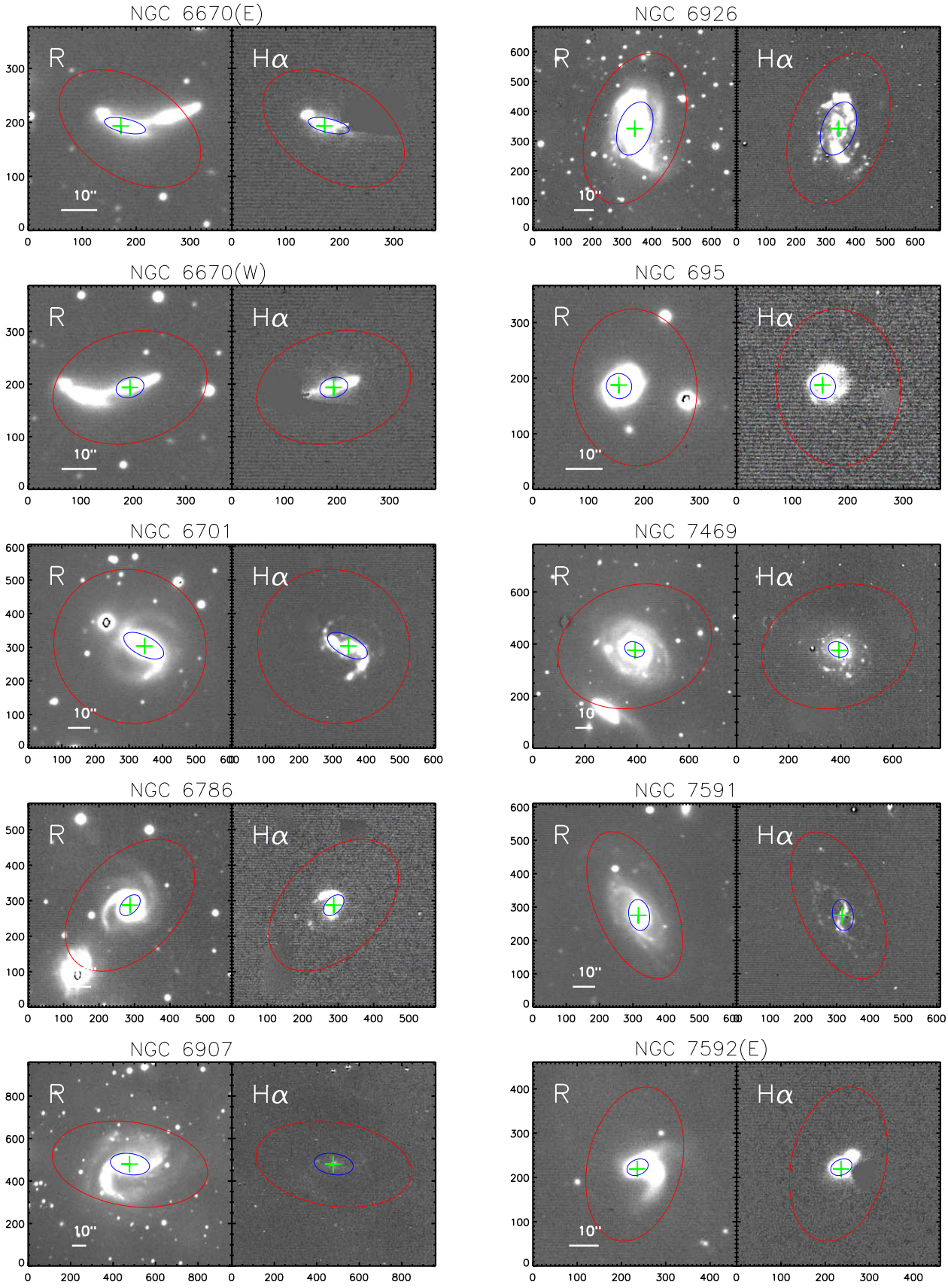

Figure 16. (Continued.)

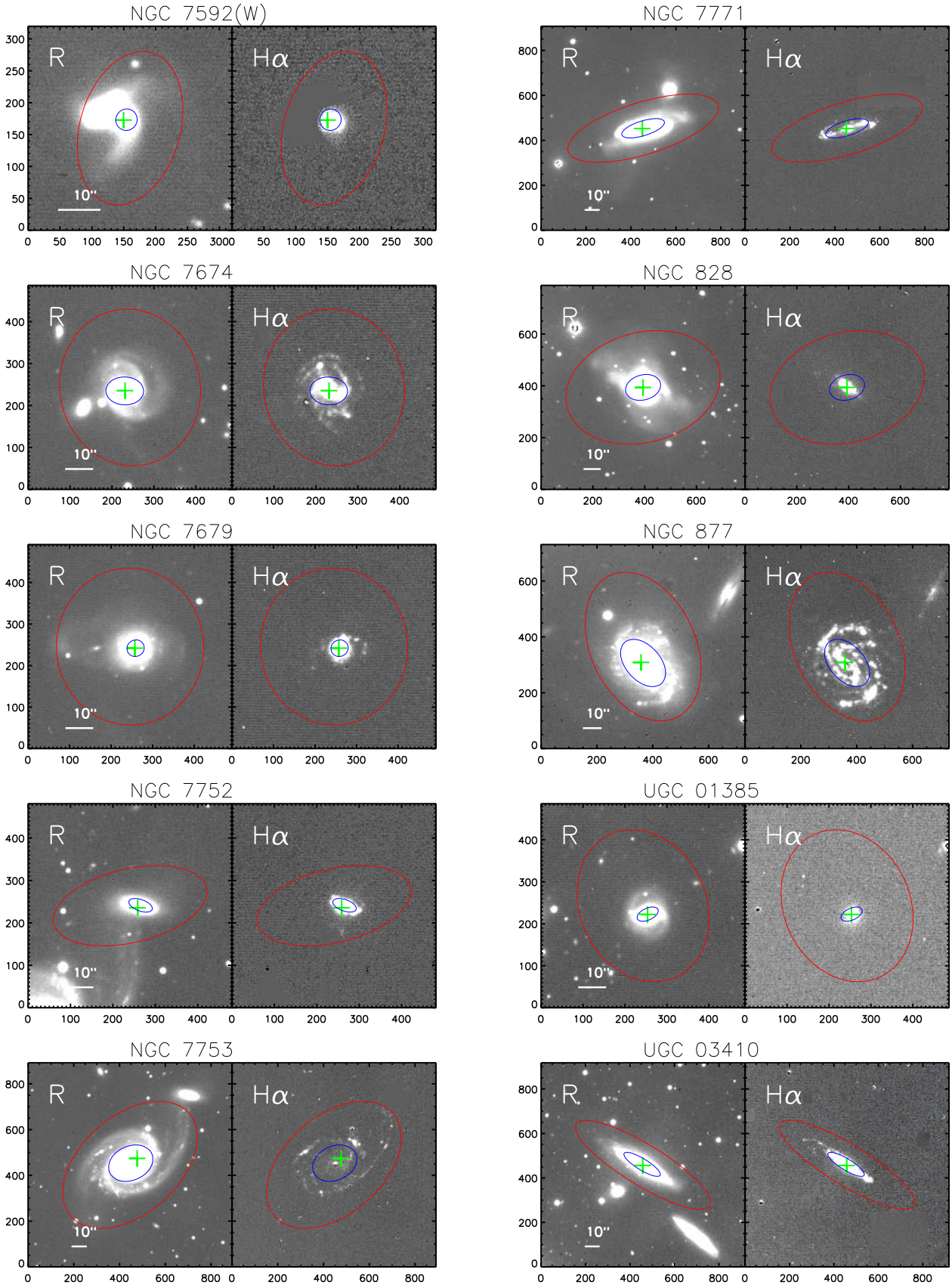

Figure 16. (Continued.)

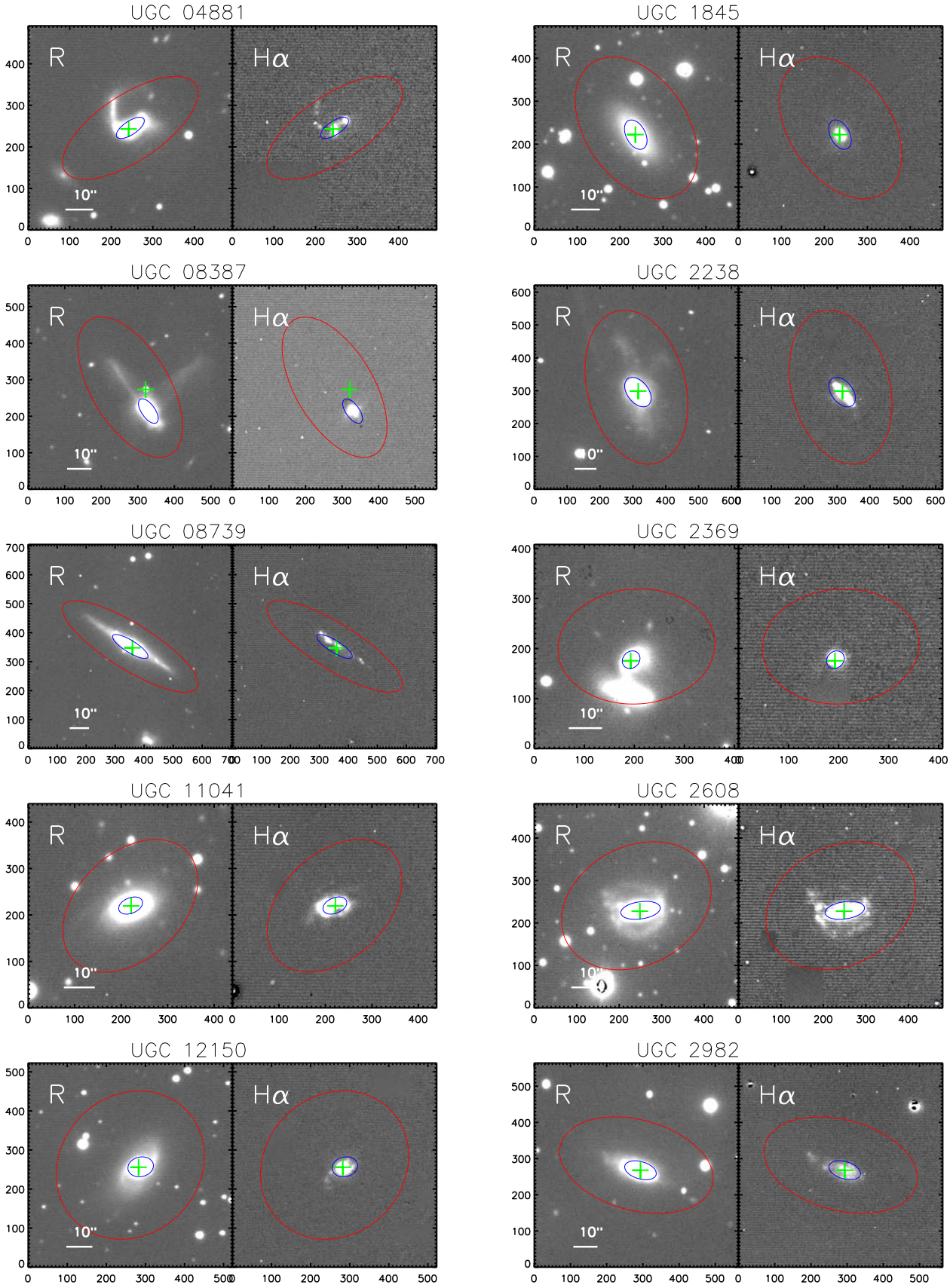

Figure 16. (Continued.)

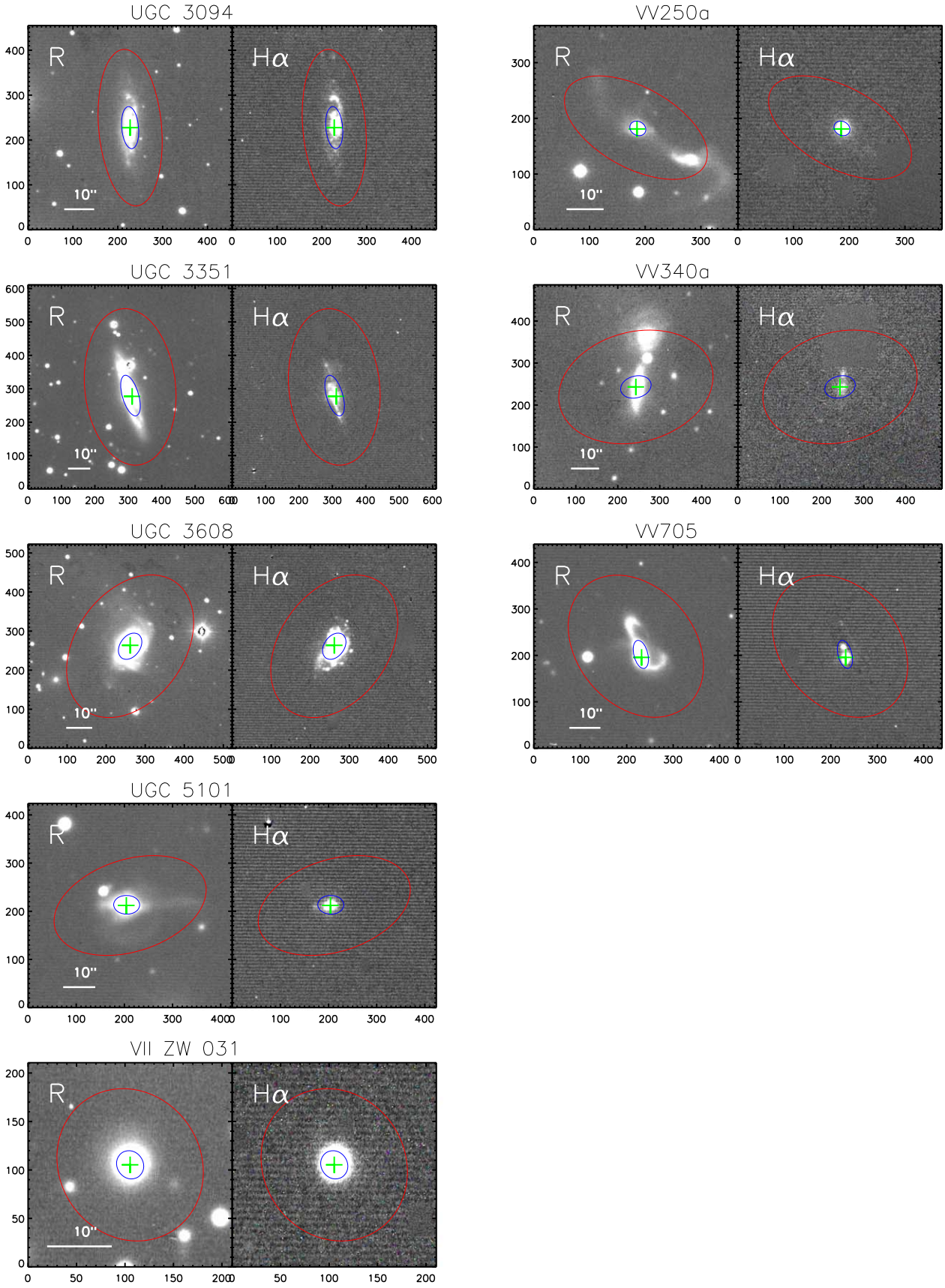

Figure 16. (Continued.)

Appendix B
Controversial Source of Morphological Classification

In this appendix, we provide further details and discussion for the classification of eight objects that are not exactly matched with L16 or K13. We will state why our classification differs from L16 or K13 and the reasons for our classification. The images for these objects are provided in Figure 17.

IRAS F01364-1042, classified as E in our work, is based on the detection of a single compact nucleus, and there are no signs of tides that can be distinguished in our image. This object is classified as M3 in L16 based on a disturbed disk with a small projected nuclear separation. The difference between these two classifications is due to the difference in resolution, and ultimately, we retain our original decision for consistency among our sample.

CGCG 052-037, classified as LM in our work, seems to have some tidal structure in this galaxy. This object is classified as s in L16 based on its appearance as a single object with no clear sign of interaction. The difference in classification for this object is more subjective.

ESO 602-G025, classified as M in our work, seems have some interaction structure that may be due to a minor merger with a small galaxy. This object is classified as s in L16 based on that they think there is no clear sign of an interaction. The difference in classification for this object is more subjective.

UGC 2982, classified as LM in our work, is based on its tidal structure. This object is classified as s in L16. Combined with the Hα image, we believe that this object is more likely to be in an interaction.

IC 5298, classified as LM in our work, is based on single nucleus with faint tidal tail. This object is classified as 0 (a single undisturbed galaxy, showing no signs of tidal interaction) in K13. In L16, this object is classified as m (minor merger). They think there is a small companion in SW and that they are connected together with a tidal tail. In a way, our result is consistent with L16.

IRAS 20351+2521, classified as M in our work, is based on its clearly disturbed disk. L16 do not include this object, and K13 classify this object as 0.

IRAS F17138-1017 is not contained in the work of L16. We classify this object as M based on it being a disturbed disk. But K13 classify this object as 0. The difference in classification for this object is more subjective.

NGC 695, classified as M in our work, is based on its disturbed disk. This object is classified as 0 in K13. In L16, this object is classified as m (minor merger). They think there is a

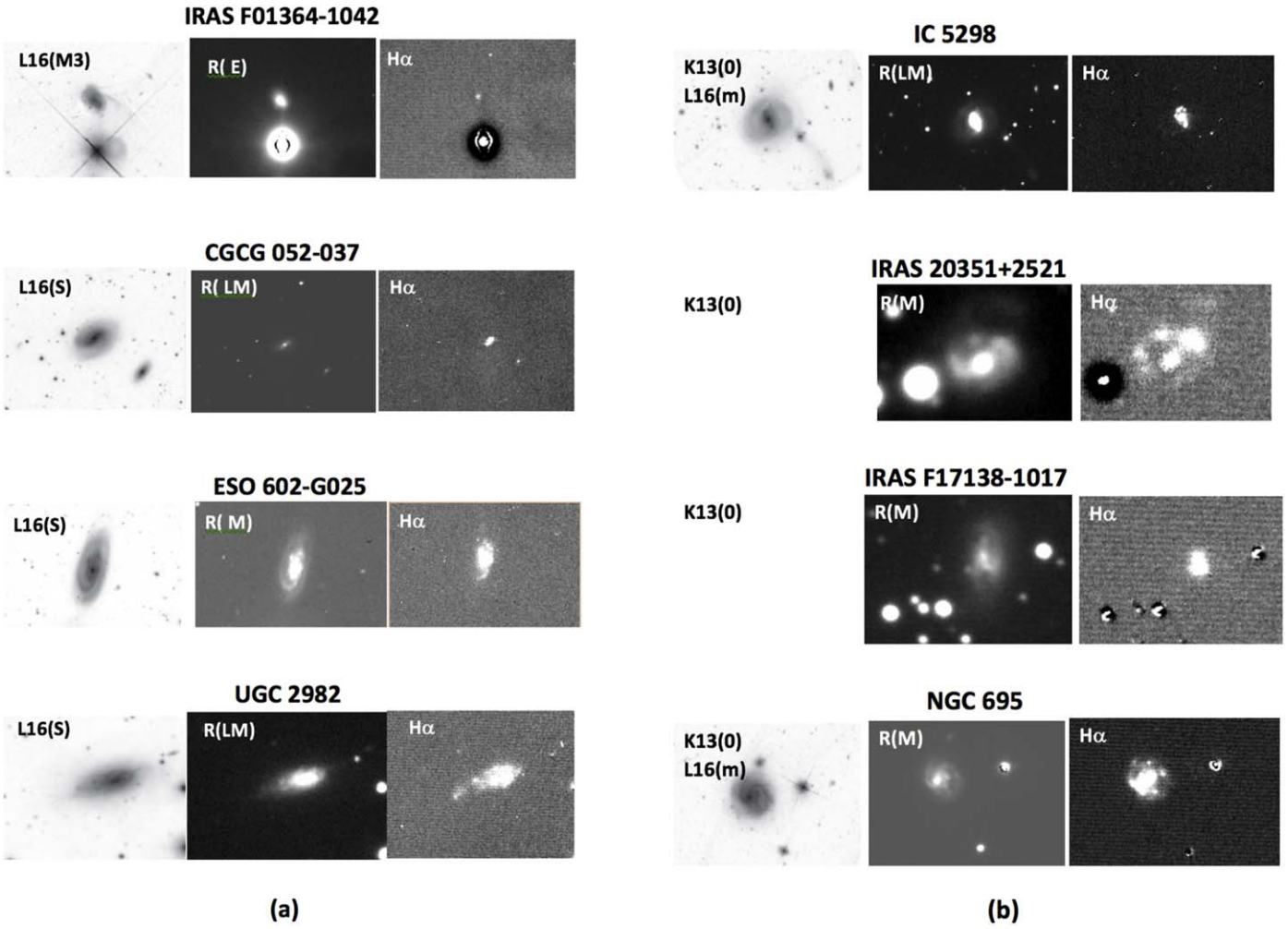

Figure 17. Details and justifications for the classification of objects that require a change greater than a single stage when compared with L16 and K13. Panel (a) lists the objects compared to L16, and panel (b) lists the objects compared to K13. The left image in each row is derived from L16 (IRAS 20351+2521 and IRAS F17138-1017 do not have the images from L16), and the classification types made by L16 or K13 are marked. The middle image is the *R*-band image in this work, and the classification types of this work are marked. The right image is the Hα image in this work.

minor companion NW of the main galaxy along with the appearance of a tidal perturbation. In a way, our result is consistent with L16.

ORCID iDs

Jun-Jie Jin https://orcid.org/0000-0002-8402-3722

References

Armus, L., Mazzarella, J. M., Evans, A. S., et al. 2009, PASP, 121, 559
Barnes, J. E., & Hernquist, L. 1992, ARA&A, 30, 705
Barnes, J. E., & Hernquist, L. 1996, ApJ, 471, 115
Barnes, J. E., & Hernquist, L. E. 1991, ApJL, 370, L65
Bryant, P. M., & Scoville, N. Z. 1999, AJ, 117, 2632
Cao, C., Wu, H., Wang, J.-L., et al. 2006, ChJAA, 6, 197
Chu, J. K., Sanders, D. B., Larson, K. L., et al. 2017, ApJS, 229, 25
Cui, J., Xia, X.-Y., Deng, Z.-G., Mao, S., & Zou, Z.-L. 2001, AJ, 122, 63
Du, W., Wu, H., Lam, M. I., et al. 2015, AJ, 149, 199
Fan, Z., Wang, H., Jiang, X., et al. 2016, PASP, 128, 115005
Fitzpatrick, E. L. 1999, PASP, 111, 63
Frei, Z., & Gunn, J. E. 1994, AJ, 108, 1476
Gavazzi, G., Fumagalli, M., Galardo, V., et al. 2012, A&A, 545, A16
Haan, S., Surace, J. A., Armus, L., et al. 2011, AJ, 141, 100
Hattori, T., Yoshida, M., Ohtani, H., et al. 2004, AJ, 127, 736
Helou, G. 1986, ApJL, 311, L33
Hernquist, L., & Mihos, J. C. 1995, ApJ, 448, 41
Hopkins, P. F., Hernquist, L., Cox, T. J., & Kereš, D. 2008, ApJS, 175, 356
Hwang, C.-Y., Lo, K. Y., Gao, Y., Gruendl, R. A., & Lu, N. Y. 1999, ApJL, 511, L17
Ishida 2004, PhD thesis, Univ. Hawaii
Jin, J.-J., Zhu, Y.-N., Meng, X.-M., Lei, F.-J., & Wu, H. 2018, ApJ, 864, 32
Kennicutt, R. C., Jr., Hao, C.-N., Calzetti, D., et al. 2009, ApJ, 703, 1672
Kennicutt, R. C., Jr., Keel, W. C., van der Hulst, J. M., Hummel, E., & Roettiger, K. A. 1987, AJ, 93, 1011
Kim, D.-C. 1995, PhD thesis, Univ. Hawaii
Kim, D.-C., Evans, A. S., Vavilkin, T., et al. 2013, ApJ, 768, 102
Kim, D.-C., Veilleux, S., & Sanders, D. B. 2002, ApJS, 143, 277
Lam, M. I., Wu, H., Yang, M., et al. 2015, RAA, 15, 1424
Larson, K. L., Sanders, D. B., Barnes, J. E., et al. 2016, ApJ, 825, 128
Lei, F.-J., Wu, H., Du, W., et al. 2018, ApJS, 235, 18
Lutz, D. 1992, A&A, 259, 462
Melbourne, J., Koo, D. C., & Le Floc'h, E. 2005, ApJL, 632, L65
Mihos, J. C., & Bothun, G. D. 1998, ApJ, 500, 619
Mould, J. R., Huchra, J. P., Freedman, W. L., et al. 2000, ApJ, 529, 786
Oke, J. B., & Gunn, J. E. 1983, ApJ, 266, 713
Reddy, N. A., Steidel, C. C., Fadda, D., et al. 2006, ApJ, 644, 792
Rigopoulou, D., Spoon, H. W. W., Genzel, R., et al. 1999, AJ, 118, 2625
Sanders, D. B., Mazzarella, J. M., Kim, D.-C., Surace, J. A., & Soifer, B. T. 2003, AJ, 126, 1607
Sanders, D. B., & Mirabel, I. F. 1996, ARA&A, 34, 749
Sanders, D. B., Soifer, B. T., Elias, J. H., et al. 1988, ApJ, 325, 74
Schlegel, D. J., Finkbeiner, D. P., & Davis, M. 1998, ApJ, 500, 525
Scoville, N. 2001, in ASP Conf. Ser. 235, Science with the Atacama Large Millimeter Array, ed. A. Wootten (San Francisco, CA: ASP), 281
Sekiguchi, K. 1987, ApJ, 316, 145
Springel, V., Di Matteo, T., & Hernquist, L. 2005, MNRAS, 361, 776
Theios, R. L., Malkan, M. A., & Ross, N. R. 2016, ApJ, 822, 45
Tonry, J. L., Stubbs, C. W., Lykke, K. R., et al. 2012, ApJ, 750, 99
Toomre, A. 1977, ARA&A, 15, 437
Toomre, A., & Toomre, J. 1972, ApJ, 178, 623
van Dokkum, P. G. 2001, PASP, 113, 1420
Veilleux, S., Kim, D.-C., & Sanders, D. B. 2002, ApJS, 143, 315
Veilleux, S., Kim, D.-C., Sanders, D. B., Mazzarella, J. M., & Soifer, B. T. 1995, ApJS, 98, 171
Wang, J. L., Xia, X. Y., Mao, S., et al. 2006, ApJ, 649, 722
Watson, L. C., Martini, P., Lisenfeld, U., Böker, T., & Schinnerer, E. 2016, MNRAS, 455, 1807
Wu, H., Burstein, D., Deng, Z., et al. 2002, AJ, 123, 1364
Wu, H., Zou, Z. L., Xia, X. Y., & Deng, Z. G. 1998a, A&AS, 127, 521
Wu, H., Zou, Z. L., Xia, X. Y., & Deng, Z. G. 1998b, A&AS, 132, 181
Xia, X. Y., Xue, S. J., Mao, S., et al. 2002, ApJ, 564, 196
Xu, C., Gao, Y., Mazzarella, J., et al. 2000, ApJ, 541, 644
Young, J. S., Allen, L., Kenney, J. D. P., Lesser, A., & Rownd, B. 1996, AJ, 112, 1903
Zheng, X. Z., Hammer, F., Flores, H., Assémat, F., & Pelat, D. 2004, A&A, 421, 847
Zheng, Z., Shang, Z., Su, H., et al. 1999, AJ, 117, 2757
Zheng, Z., Wu, H., Mao, S., et al. 1999, A&A, 349, 735
Zhu, Y.-N., Wu, H., Cao, C., & Li, H.-N. 2008, ApJ, 686, 155
Zou, Z., Xia, X., Deng, Z., & Su, H. 1991, MNRAS, 252, 593